Unraveling the single cell spatial landscapes of melanoma brain metastases

Artür Manukyan[1,*,§], Kristin Peters[2,*], Helena Radbruch[3], Florian Rossner[4], Annika Lehmann[4], Karsten Kleo[4], Thomas Conrad[5,6], Janine Altmüller[5,6], Izabela Plumbom[5,6], Altuna Akalin[1], Karsten Jürchott[7], Emanuel Wyler[1], Markus Landthaler[1,8], Josefine Radke[2,9,#,§], Torben Redmer[9,10,#,§]

[1]Max Delbrück Center for Molecular Medicine in the Helmholtz Association (MDC), Berlin Institute for Medical Systems Biology, Berlin, Germany

[2]Institute of Pathology, University Medicine Greifswald, Greifswald, Germany

[3]Institute of Neuropathology, Charité – Universitätsmedizin Berlin, Corporate Member of Freie Universität Berlin and Humboldt-Universität zu Berlin, Berlin, Germany

[4]Institute of Pathology, Charité – Universitätsmedizin Berlin, Corporate Member of Freie Universität Berlin and Humboldt-Universität zu Berlin, Berlin, Germany

[5]Genomics Technology Platform, Max Delbrück Center for Molecular Medicine in the Helmholtz Association, Berlin, Germany

[6]Core Facility Genomics, Berlin Institute of Health (BIH) at Charité - Universitätsmedizin Berlin, Berlin, Germany

[7]Berlin Institute of Health (BIH) Center of Immunomics, Charité – Universitätsmedizin Berlin, Berlin, Germany

[8]Institut für Biologie, Humboldt-Universität zu Berlin, Berlin, Germany

[9]Institute of Molecular Genomics and Core Unit Genomics (CUG), University Medicine Greifswald, Greifswald, Germany

[10]Institute of Pathology, Unit of Laboratory Animal Pathology, University of Veterinary Medicine Vienna, Austria

*These authors contributed equally as first authors

[#]These authors contributed equally as senior/last authors

[§]Corresponding authors: artur.manukyan@mdc-berlin.de, josefine.radke@med.uni-greifswald.de, torben.redmer@med.uni-greifswald.de

Summary

The cellular composition that defines the tumor ecosystem plays a crucial role in determining the response of tumors to immune checkpoint inhibitors (ICi) and to pharmacological blockade of BRAF (BRAFi). However, the compositional changes that likely shape the ecosystems of primary melanomas for metastasis to the brain on the one hand and the progression of brain metastases on the other remain unclear.

In this study, we resolved the spatial landscapes of progressive melanoma brain metastases (MBM) by profiling 13 regions from 8 distinct metastases, together with one matched primary tumor spanning various stages of tumor development and therapeutic intervention. Single cell resolved spatial transcriptomics-based profiling uncovered distinct and common patterns of MBM progression. Our approach revealed remarkable cellular and spatial heterogeneity and identified key tumor subsets of MET or NGFR expressing cell populations. Moreover, spatial profiling of tumors which have progressed under ICi or BRAFi identified BZW2^{+} tumor cells contributing to an immune-suppressive microenvironment, preventing immune cell infiltration and dispersion within the tumor. Elevated BZW2 expression was associated with resistance to ICi therapy and is inversely correlated with the antigen transporter TAP1. Spatially-aware automated profiling of immune cell-enriched areas revealed “hot” niches characterized by tumor cell expression of TAP1, PD-L2, HLA-DRA whereas “cold” niches featured high levels of particularly BZW2 and SOX4. The latter suppressor of translation and transcriptional regulator was co-localized with the clinically targetable MET receptor in a subset of tumor cells that exhibit immune evasion features. In summary, we provide for the first time, spatially resolved landscapes of MBM that reveal insights into the cellular heterogeneity of tumors and the mechanisms underlying immune escape.

Keywords

Spatial biology, brain metastases, melanoma, immune suppressive programs

Introduction

Tumor development and progression are highly dynamic processes[1] that are temporally defined and driven by a complex interplay of genetic aberrations[2], environmental factors, and spatial mechanisms which in turn are regulated by communication with the tumor microenvironment (TME). While the genetic landscape of tumors provides a fundamental blueprint for their progression[3], the emergence of subclonal populations[4] and the crosstalk between tumor and stromal cells particularly involving soluble factors and extracellular vesicles[5] play crucial roles in shaping the heterogeneity and therapeutic resistance observed in cancer. The development of brain metastases is observed in 40–60% of melanoma patients during the course of the disease and, as in patients with lung and breast cancer[6] is a major contributor to disease progression and poor prognosis of patients[7-9]. In the context of brain metastases, astrocytes, oligodendrocytes and tumor-associated macrophages (TAMs) are the most important tumor cell interactors and contribute to the establishment of distinct tumor niches in the brain[10]. These in turn facilitate the maintenance and progression of metastatic tumor cells, hence determining the course and routes of development from initially small and asymptomatic brain micrometastases to symptomatic macrometastases[10] through intricate signaling networks[11].

Currently, therapeutic targeting of the PD-1/PD-L1 axis or LAG-3 interactions with neutralizing antibodies represents one of the most important strategies for restoring T cell activation and enabling tumor cell recognition and elimination[12]. Despite a subset of patients showing complete intracranial response (CR) to ICi, immune resistance programs (IRPs) evolve in the majority of patients and hence determine the clinical response of MBM to anti-PD-1 therapy[13,14]. Likely, environmental stresses induced by BRAFi targeting the mutated and hyperactivated BRAF kinase ($BRAF^{V600E/K/R}$) or ICi both aiming to block tumor growth can also remodel the TME and alter the dynamics of tumor-stromal interactions[15]. These observations highlight the complexity of the TME and underscore the limitations of current therapies in overcoming the tumor's ability to evade the immune system and develop therapy resistance.

Previous studies identified gene signatures predicting the response of melanoma to ICi[13,16,17], among them a tumor-intrinsic NGFR (nerve growth factor receptor)-associated gene signature predicting anti-PD-1 therapy resistance[18]. However, signature genes likely reflect multiple concerted molecular mechanisms of immune cell (T cell) suppression, involving potentially interacting tumor and stroma cell-associated mechanisms. The insufficient immune cell infiltration into MBM remains a major barrier to effective therapy.

Epithelial-like MBM, characterized by expression of Ecad (CDH1), adopt an $NGFR^+$ cell phenotype in response to antigen-specific cytotoxic T cells[18] or therapeutic interventions[19].Hence, only a minority typically early-stage or therapy-naïve tumors might exhibit high levels of immune cell infiltration[20]. Therefore, ICi therapy might be ineffective in MBM featuring low levels of tumor immune cell infiltration and IFNγ scores[20] besides low PD-L1 expression[21]. The efficacy of immune checkpoint inhibitor (ICi) therapy is likely influenced by additional, predominantly spatially regulated mechanisms, such as the presentation of tumor antigens to adjacent immune cells[22]. Moreover, the different developmental stages and molecular phenotypes of MBM, likely determine the response to therapeutic interventions and the transition from a tumor growth suppressive to an inflammatory and progressively evolving microenvironment that promotes tumor growth and metastasis[23].

Brain metastases likely consist of spatial areas with varying levels of sensitivity and resistance to therapy, posing a major challenge to the development of more effective treatments. To address these challenges, we have employed spatial transcriptomic profiling to investigate the molecular landscapes of MBM (n=16) including whole sections of matched primary and brain metastasis (total n=2) and primary and relapsed MBM (total n=2). Moreover, we investigated the methylome-based copy number variation (CNV) profiles of progressive tumors (n=4). Here, we present single cell and spatially resolved landscapes of MBM of diverse therapeutic and developmental stages.

Results

BZW2 and TAP1 discriminate immunologic niches in MBM

Immune checkpoint inhibitors (ICi) achieved durable responses and improved survival in advanced-stage melanoma patients[24]. However, only small and asymptomatic brain metastases were susceptible to disease control[14,25]. The formation of spatially defined immunosuppressive areas probably accompanies tumor development and intrinsically determines ICi-resistant areas within larger tumors.

We evaluated the representation of immune suppressive programs which potentially mediated resistance of MBM to ICi therapy. To this end, we surveyed bulk expression data of MBM and brain control samples (BC) of our previous study[19]. A pan-MBM gene signature was revealed by comparing MBM with BC samples from non-cancer autopsies to subtract genes only expressed in adjacent CNS tissue. Comparison of previously identified IRP and pan-MBM signature genes[13] revealed 59 MBM expressed IRP genes (Figure S1a, Table S1). Gene set enrichment analysis (GSEA) illustrated the extent of enrichment of potential suppressors and activator of immune response in MBM, hence representing the “on-off” status of immune resistance. As expected, GSEA revealed enrichment of genes of both molecular programs (Figure S1b). We identified the regulators of translation and transcription BZW2[26] and SOX4[27] serving as potential mediators of IRP in MBM. BZW2 and SOX4 were predominantly expressed in MBM and MBM-derived cell lines (BMCs), but not in BC samples (Figure S1c), similar to the recently identified immune suppressor CDK4. A survey of scRNAseq data of ICi responsive and refractory melanoma (GSE115978)[13] revealed increased levels of BZW2 and SOX4 in post-treatment tumors (Figures 2a, 2b and S1d), with no obvious relation to PD-L1 expression (Figure S1e). The correlation of ICi-related disease progression stages with the tumor´s expression profile provides insights into response-determining mechanisms. We observed that BZW2, but not SOX4, is associated with the response of melanoma to ICi. BZW2 was increased in patients with progressive (PD) or partially responding disease (PR) and significantly ($p < 0.05$) discriminated patients who

showed a complete (CR) or PR (Figure 2c). In contrast, we observed a significant reduction in the levels of the peptide transporter TAP1 which mediates the translocation of peptide antigens for loading onto MHC class I molecules such as HLA-A (Figure S1f)[28]. In concordance, melanoma patients with tumors expressing high levels of BZW2 (HR=1.55, logrank P=0.0011) and SOX4 (HR=1.52, logrank P=0.0019) showed unfavorable overall survival (OS, TCGA-SKCM, n=459). TAP1 expression on the other hand was associated with favorable OS (HR=0.45, logrank $P=4.4x10^{-6}$) (Figure S1g).

Tumor ecosystems can change over time, either evolving phenotypes that are intrinsically resistant to ICi therapy or developing immune resistance in response to ICi therapy. We applied spatial transcriptomics using the Xenium in situ profiler (10X Genomics) to investigate the spatial composition of individual cells in ICi-resistant or cross-resistant “cold” areas and in ICi-sensitive and potentially “hot” niches by profiling 13 regions from 8 distinct metastases, together with one matched primary tumor spanning various stages of tumor development and therapeutic intervention. We annotated single cells by performing downstream unbiased clustering analysis of Xenium single cell RNA profiles, followed by the automated alignment of post-Xenium H&E images.

We first investigated an NRAS ($NRAS^{Q61L}$)-mutated primary mucosal melanoma (mM) that was first diagnosed in the nasal cavity in 2021. The tumor showed progression to the frontotemporal lobe of the brain under ICi therapy and was resected 4 months after ICi was terminated (Figure 2d, Figure S2a). The spatial mapping of the primary mM and of the concordant mMBM allowed analysis of ~410,000 cells and ~290,000 cells respectively and revealed landscapes comprising up to 12 different tumor cell subtypes (TCs), infiltrated tumor-associated macrophages/microglia (TAMs), immune cells, proliferating/cell cycle progressing cells, vascular-leptomeningeal cells and cancer-associated fibroblasts (VLMC/CAFs) as well as adjacent epithelial cells (CDH1/$Ecad^{+}$, $CXCL14^{+}$) of the primary mM and MBM-associated astrocytes ($GFAP^{+}$), (Figures S2b, c). Additionally, we identified a rare $SLC17A6^{+}$ (glutamate transporter) cellular subset of uncertain prognostic relevance which

was unique to the primary tumor but depleted in the MBM. Moreover, we observed well-defined and spatially separated areas of enrichment or depletion of immune cells. Immune cells were predominantly enriched at sites of high tumor cell expression of TAP1 (Figure 2e and Figure S2b, c; TCs_4, Table S2). By contrast, high BZW2 expression was observed in tumor cells located in immune cell-depleted areas (Figure 2e and Figure S2b, c; TCs_7, TCs_8, Table S2). Identifying the top-expressed genes characteristic of each cell type cluster enabled accurate classification and a better understanding of the cell types. Immune suppressive BZW2^{+} cells showed cellular heterogeneity and accompanied co-expression of SOX4 and BCAN or CD93 (TCs_7, TC_8; Table S2; Pat 90 primary mM) and TAP1^{+} tumor cells co-expressed STAT1 among additional markers (Figure S2c, Supplementary table 2; Pat 90 primary mM). Furthermore, we observed that the proportions of the major cell types reflected changes in cellular composition that likely occurred during the progression of brain metastases (Figure S2d, left panel).

Spatial profiling enabled the characterization of immunogenic niches

Based on the results obtained so far, we hypothesized that TAP1 and BZW2 play antagonistic roles in regulating immune cell infiltration. Therefore, we examined the changes in cellular composition associated with the spread of tumor cells into the brain, focusing on the persistence of immune suppressive BZW2^{+} and immune supportive TAP1^{+} areas in the resulting mMBM.

The comparative spatial mapping revealed loss of immune suppressive BZW2 areas but maintenance or emergence of TAP1^{+} areas in the brain metastasis (Figures 2g and S2d, right panel). In addition to the spatial mapping of individual genes, we sought to investigate the spatial distribution of areas with a high abundance of immune cells, represented by the immune score (IS). The IS was calculated in two ways, using the ESTIMATE signature, which includes predefined genes associated with immune cell infiltration and activation[29]. IS

determined from pseudo-bulk data using single-sample gene set enrichment analysis (ssGSEA) provided insights into the total immune cell content, but only spatial mapping of values assessed using the AddModuleScore function from Seurat (Table S3) revealed immunogenic niches, even in tumors with low total IS.

Consistent with the loss of BZW2^{+} cells, we observed that IS^{high} areas largely coincided with TAP1 expression (Figure 2h). Furthermore, we observed mutual exclusivity of TAP1 expression and lowest immune scores within BZW2^{+} tumor cell-enriched niches (Figures 2g, h).

We have performed hot spot analysis using VoltRon[30] toolbox to detect local microenvironments with IS^{high} cells (STAR Methods). Here, the method automatically labels each cell as “hot” if the Getis-Ord test[31] is found significant for that gene, indicating that the cell is within proximity to a region abundant with IS^{high} cells, and labelled as “cold” otherwise. Considering the various stages of development, it is likely that immunogenic (“hot”) and suppressive (“cold”) niches evolve and deplete over time and along progression which was evident by automatically niche mapping (Figure 2i, left panels and Figure S3), hence determining the tumor landscapes and therapy responses. We observed that TAP1^{+} tumor cells were the main contributors of immunogenic niches, however only a subset of niche-supportive tumor cells were maintained during brain metastasis or in the establishment of the brain tumor (Figure 2i, right panels and Figure S3). Moreover, we found general (other) markers which not significantly classified niches. In order to identify valid markers that characterize cold and hot niches independently of the tumor’s mutation and therapeutic status, we performed differential expression (DE) analysis (see STAR-Methods) of the previously defined TAP1^{+} tumor cell niches surrounding IS clusters (group of cells with high IS). Differential expression analyses of tumor cells alone or of tumor cells and environmental cells (TME) of aggregated niches across TMA samples and whole tumors validated TAP1, HLA-DRA, PD-L2 (PDCD1LG2) and ITGB2 as major contributors of immunogenic niches (Figure 2j, upper row). In contrast, BZW2, PSENEN, SOX4 and SOX6 served as main

mediators of an immune suppressive environment (Figure 2j, upper lower row). In addition to single genes, we applied state-predictive gene signatures for calculation of scores (Table S5) and observed significant enrichment of immune-related molecular programs, particularly ESTIMATE, Roh, IPRES (innate PD-1 inhibitor resistance[32]) and NRS (Neoadjuvant Response Signature[17]) in “hot” niches. In addition to immune cells, we observed a significant enrichment of TAMs expressing C1QC, TMIGD3 and AIF1 in immune “hot” niches. The comprehensive niche profiling uncovered differential niche-dependent regulation of additional, immune cell-specifying signatures and revealed NGFR-related programs unrelated to $BZW2^+$/$SOX4^+$-associated immune suppressive niches (Table S5). In line with our data, we suggest that immunogenic niches comprise an immune cell and TAM enriched core which is surrounded by $TAP1^+$ tumor cells embedded into the $BZW2^+$ suppressive environment (Figure 2k, upper scheme). The model is supported by the distance of $TAP1^+$ and $BZW2^+$ tumor cells to the nearest immune cell as defined by expression of a gene signature which includes markers such as CD3G, CD8A, CD4, TRAC and PTPRC among others. Proximity calculation across all niches revealed an average distance of 4.2(±0.9) µm and 5.8(±1.0) µm of $TAP1^+$ cells (n=61,071) and $BZW2^+$ cells (n=146,947) to the nearest immune cell (Figures 2k, lower scheme and 2l; Table S6), respectively.

Despite the robust separation of these niches, TAP1 and the MHC class II molecule HLA-DRA are expressed by both tumor cells and immune cells, including activated T cells[33,34]. Along with other markers, this expression facilitates the immune response[35]. Tumor cell-expressed TAP1 is essential for the presentation of tumor antigens enabling recognition by immune cells. Therefore, TAP1 deficiency is associated with a lack of cytotoxic $CD8^+$ T cells[36]. Consequently, the down regulation of TAP1 in tumor cells serves as an important mechanism of immune evasion[37]. On the other hand, the absence of TAP1 expression in T cells severely impairs antigen presentation, particularly the presentation of cytosolic antigens to class I-restricted cytotoxic T cells results in reduced surface expression of MHC class I molecules and an absence of mature $CD8^+$ T cells[36,38]. Within the immune cell cluster, we

identified putatively activated cytotoxic T cells characterized by the expression of TRAC and HLA-DRA, in addition to TAP1 and CD8A (Figure 2m, right panel).

Spatial mapping of the cellular subgroups of the primary mM and the corresponding metachronously developed mMBM provided insights into the changes in the cellular composition of the tumors that were likely associated with metastatic progression. We observed that TAP1 and BZW2 expressing “hot” and “cold” niches were maintained or re-established during mMBM formation and progression. Moreover, we observed a minor cell population exhibiting high expression of BZW2, low TAP1 expression and depletion of $TRAC^{+}$ T cells (Figure 2n). Generally, levels of BZW2 and SOX4 were reduced in MBM (Figure S2e). In concordance with reduced expression of immune suppressive molecules, we observed higher immune scores and enrichment of $CD8A^{+}$ T cells in MBM (Figure S4a). To assess the extent of global changes that may occur during metastatic progression we performed methylome-based copy number variation analysis using the EPICv2 (930k) technology. We observed amplification of several genes on chromosome 7, including the MET receptor (Figure S4b). FISH (fluorescence in-situ hybridization) analysis validated the amplification of MET and of chromosome 7 (CET7) in mMBM (Figure S4c, Table S7).

In summary, the comparative spatial profiling of matched primary mM and MBM revealed that BZW2 and TAP1 define distinct areas which potentially support or suppress immune cell infiltration and activation. Despite the changes in tumor ecosystems occurring alongside brain metastatic progression of the primary tumor, immune cell suppressive and supportive niches were restored in the MBM. The $BZW2^{+}/TAP1^{low}$ cells may be prone to metastasize to the brain.

The presence of immune niches is associated with an active interferon response

Our previous results suggest that BZW2 and TAP1 serve as markers distinguishing immunogenic niches in melanoma (Figure 3a), however not excluding intermediate states

showing co-expression of both determinants of immune surveillance. In order to assess the relevance of these genes and tumor states, we investigated survival probabilities of melanoma patients featuring distinct high or low or co-expression of TAP1 and BZW2. We indeed observed the highest survival probability of patients (TCGA-SKCM, n=459) featuring $BZW2^{low}/TAP1^{high}$ expression and lowest survival probability of $BZW2^{high}/TAP1^{low}$ patients (Figure 3b). This suggests that the presence of TAP1 serves as an indicator of favorable prognosis depending on the level of BZW2. Therefore, TAP1 and BZW2 could serve as novel prognostic biomarkers for the survival of melanoma patients.

The separation of patient groups was even more evident with regards to the levels of HLA-DRA. Patients with high levels of HLA-DRA exhibited the most favorable prognosis; however, co-expression of BZW2 attenuated this beneficial effect (Figure S4a). In concordance to our previous observation, TAP1 expression served as a potential prognostic marker suggesting a higher survival probability of melanoma patients with $TAP1^{high}$ MBM (Figure S4b). Next, we thought of identifying genes that may define the molecular states of $BZW2^{+}$ or $TAP1^{+}$ cells. To unravel the potential global networks associated with BZW2 and TAP1, we determined the differentially expressed genes of $TAP1^{high/low}$ and $BZW2^{high/low}$ tumor cells (malignant cells) from whole transcriptome gene expression of treatment-naive MBM (GSE200218) (Figure 3c and Figure S4c). $TAP1^{high}$ cells showed co-expression of interferon (IFN)-associated genes such as IFI6. In contrast, $BZW2^{high}$ cells were particularly enriched for CHL1 (Cell Adhesion Molecule L1 Like) and CTNNA2 (Catenin Alpha 2) (Figure 3d, Table S8). Suggesting a correlation of niches of $TAP1^{+}$ cells and interferon signaling, we found the downstream mediator of IFNα/β signaling MX1 and the target of IFNγ signaling LGALS9 significantly higher expressed in “hot” spatial niches (Figure 3e) and showed a moderate correlation (Figure 3f, left panel). In order to establish a role of IFN signaling (Figure 3f, right panel) for the possible emergence and maintenance of immune cell-enriched niches, we spatially mapped the expression of IFI6 (Interferon Alpha Inducible Protein 6) on primary mucosal melanoma (Figure 3g, left panel).

The mapping of major cell types to discrete IFI6^{high} areas revealed an immune (T) cell niche in the primary tumor which was embedded into a well-organized microenvironment of tumor cell subsets (TCs_3, TCs_7, Table S2) and interferon expressing tumor cells (Figure 3g, second left panel). The analysis of tumor cell types revealed co-occurrence of TRAC^{+} T cells and interferons MX1 and IFI6 and showed a clear separation of BZW2^{+} and TAP1^{+} niche cells and a potential key role of the IFN signaling pathway (Figure 3g, right and second right)[39]. Considering the complex process of metastasis and the unique environment of the brain[40], we investigated the mediators of interferon signaling in the brain metastatic (Secondary immune niche) immunogenic niche. Albeit less abundant, we observed hot spots of IFI6 expression in the mMBM (Figure 3h, left panel). The cell type analysis of the secondary immune niche uncovered a tumor subtype-specific enrichment of immune (T) cells (Figure 3h, second left panel). The classification of cellular subtypes demonstrated the mutual exclusivity of expression of interferons and BZW2 and showed once more the association of TAP1^{+} and enrichment of TRAC^{+} cells in TAP1^{+}/MX1 or TAP1^{+}/IFI6^{+} areas (Figure 3h, right panels). The loss of TAP1 expression in tumor cells may be the consequence of genetic aberrations or defects in inducing signaling pathways such as IFN signaling[41,42]. The signal transducer and activator of transcription 1 (STAT1) and STAT2 serve as key factors of interferon signaling[39]. This suggests a lack of STAT1 expression in immune-repressive or “cold” BZW2^{+} tumor cells, with BZW2^{high}/STAT1^{low} melanoma patients exhibiting the lowest overall survival (Figure S4d).

We found STAT1 spatially co-expressed particularly at TAP1^{high} sites of primary mM and mMBM (Figure 3i left panel, Figure S4e, Table S2) and associated with enrichment of T cells (TRAC^{+}) (Figure S4f). In contrast to STAT1, we observed overlapping rather than mutually exclusive patterns of spatially expressed SOX4 and MET and to a lesser extent, PSENEN (Figures S4g, h). MET was co-localized with BZW2 at restricted areas within the mMBM (Figure S5a). Immunohistochemistry validated STAT1 and HLA-DR(A) expression at TAP1^{+} areas and showed sites of low or absent expression of both markers of immune supportive

areas (Figure 3i, center panels and Figure S5b). Here, we provide evidence that BZW2 not only shows mutually exclusivity with TAP1 but demonstrated that low STAT1, MX1 and IFI6 levels were associated with high BZW2 expression, suggesting that BZW2 may be associated with suppression of STAT1-mediated signaling, which in turn drives TAP1 expression. In line we observed that TAP1 and STAT1 showed association with a comprehensive immune-associated protein interaction-network among them the immune proteasomes PSMB8/9, major histocompatibility complex class I genes and interferon-inducible genes e.g. IFI6 (Figure S5c).

BZW2/TAP1-associated programs function across MBM of different therapeutic stages

Therapeutic interventions likely foster selection of cellular subsets featuring minimal residual disease (MRD)[43,44], suggesting that MBM which have been developed under therapy may comprise drug resistant, stem-like cells. We performed a thorough analysis of TMA samples for identification of the spatial single cell heterogeneity of MBM across different patients who received BRAFi and/or ICi therapy (Figures 4a upper scheme, S6a, Table S3) and to investigate the distribution and occurrence of BZW2 and TAP1 in niches across multiple progression stages. Unbiased clustering of Xenium cells followed by automated H&E image alignment (see STAR Methods) revealed distinct and common proportions of cellular sub clusters regarding the molecular phenotypes (e.g. Ecad^{+}, NGFR^{+}, MET/SOX4^{+}) and separation of tumor cells from CNS tissue and from primary CNS lymphoma (PCNSL) (Figures 4a lower panel and 4b, S6b-c). Despite the different origins and developmental strategies of MBM and PCNSL both malignancies likely accompany restructuring of the brain environment. The comparison enables us to disentangle tumor-intrinsic factors from microenvironmental cues driving tumor progression and immune evasion.

Tumor specimen revealed pronounced intertumor and intratumor heterogeneity showing distinct and overlapping expression of markers specifying different tumor cell clusters,

immune cells, TAMs, endothelial cells and CAFs (Table S2). Marker analysis of clusters and joint interactive visualization of cells via H&E images enabled the annotation of tumor cell subtypes (TCs, cycling TCs, NGFR^{+}) and non-tumor subtypes (immune cells, TAMs, VLMC/CAFs, endothelial cells) and CNS-derived cells (astrocytes, oligodendrocytes, neurons) across tumor specimen and uncovered the molecular features of general cycling (MKI67/TOP2A/PCNA) and non-cycling tumor cells of NGFR^{+} subsets (Figure 4b, c). Astrocytes and oligodendrocytes presented the major cell types of the TME. Oligodendrocytes were most prevalent in tumor-adjacent central nervous system (CNS) tissue, neurons were found at distant tumor sites or in association with micrometastases (Pat 24). Immunohistochemistry (IHC) further revealed the sub-classification of NGFR^{+}/de-differentiated/amelanotic and Ecad/melanocytic (MLANA^{+}/ HMB45^{+}) tumors (Figures S7a-b and 8a-b) and characterized the degree of immune cell infiltration, highlighting the spatial distribution of “hot” and “cold” niches (Figure S9a). All TMA tumor specimen showed infiltration of Iba1^{+} TAMs (Figure S10a).

We evaluated the TMA specimens using the immune score (IS), which indicates the degree of immune cell infiltration as calculated from pseudo-bulk expression data, and spatially mapped the expressions of BZW2, SOX4 and NGFR (IS, Table S3, Figure 4d). We observed that TMA specimen featuring high homogeneously expressed NGFR (Pat23C) or BZW2 and SOX4 (primary mucosal melanoma, Pat90-P and Pat23C) showed lowest IS. However, bulk data-derived scores only inadequately reflected the immunogenic status of tumors. The UMAP representation of deconvoluted TMA samples revealed highest levels of IS in immune cells and revealed an opposite expression pattern of BZW2 and TAP1 as well as of MET/SOX4 and HLA-DRA with no apparent correlation to therapeutic treatment strategies, but rather to molecular patterns (Figure 4e, Figure S11a-e). De-differentiation may be driven by the concerted action of BZW2/SOX4 and/or NGFR and several lines of evidence suggest an immune suppressive role of NGFR[18,45]. However, the results of our niche profiling suggested that NGFR expression may not directly contribute to BZW2- or SOX4-associated

“cold” niches. We investigated the spatial environment of an $IS^{high}/TAP1^{+}$ immune hot spot within the $NGFR^{+}$ tumor (Pat23) on single cell level (Figure 4f, left panels). We observed that the "hot" niche consisted of $TAP1^{+}/IFN^{+}/BZW2^{low}$ cells and showed enrichment of particular IFI6 (Figure S11f). In line with previous observations, we suggest that established immunogenic niches employ interferon signaling to maintain T cell subsets (Figures S11f, g)[46]. For a deeper analysis of the immune hot spot, we investigated the pattern of co-occurrence and transcript density across the cells which made up the niche. Niche-forming tumor cells showed high levels of TAP1 and HLA-DRA transcripts and low levels of BZW2 (Figure 4f, Figure S11f, g), which is probably ideal for the recognition of tumor antigens[47] by attracted and activated $CD8A^{+}$ T cells which in turn exhibited only low expression of the checkpoint markers CTLA4 and PD1 (Figures 4g-h, S12a).

In summary, spatial profiling of TMA samples confirmed the existence of immune suppressive and supportive programs associated with BZW2 and TAP1 across tumors of different therapy stages demonstrating high concordance with matched whole tumor sections which revealed high robustness in terms of the composition of niches.

Spatial profiling of MBM-adjacent CNS tissue revealed different states of inflammation

The mutual interactions of brain infiltrating tumor cells with neighboring cells, particularly astrocytes, microglia/TAMs and oligodendrocytes trigger inflammatory processes[48,49]. Recent studies in glioblastoma demonstrated that tumor-adjacent astrocytes cause an anti-inflammatory environment suppressing T cell activation[50]. The reactive states of tumor environmental cells, particularly astrocyte activation have been intensively studied in mouse models[51] and in the context of neurodegenerative diseases[51,52], however have not been studied in MBM in a spatial context. Therefore, we investigated MBM-adjacent CNS tissue for levels of AIF1/Iba1 and GFAP, well-recognized markers of activation of TAMs and astrocytes by IHC. We observed strong reactivity of TAMs at tumor distant and adjacent

areas and activation of only tumor-adjacent astrocytes (Figure S13a, b). Spatial profiling revealed a main fraction of GFAP^{+} astrocytes with at least three different subsets. Most tumor-proximal astrocytes exhibited a reactive/"A1" or neuroinflammatory phenotype (GFAP^{+}/ CHI3L1^{+}/SPP1^{+})[53,54], whereas more distal astrocytes (GFAP^{+}/GJA1^{+}/AQP4^{+}) appeared to adopt a homeostatic[47] rather than reactive[48] state (Figure S13c-f). In contrast to adjacent astrocytes and TAMs, we observed neurons (SNAP25^{+}/SYT1^{+}) nearly exclusively at distant sites and might not or at early stages primarily engage with tumor cells in MBM (Figure S13g, h).

Our survey suggests that reactive astrocyte subsets probably emerge only in response to physical interaction with tumor cells and might contribute to suppression of T cell activation.

Spatial profiling uncovered molecular programs of de-differentiation

Genetic factors and environmental cues determine the routes of tumor development and progression. Our latest results suggest that tumors comprise therapy-responsive and refractory areas both reflecting certain cellular compositions. To further unravel the cellular subsets which may support or suppress immune cell infiltration we investigated a punch of the primary mucosal melanoma-derived MBM (Pat90) which emerged over the course of four months of nivolumab/ipilimumab therapy and exhibited an extremely diverse landscape. We identified MET^{+} cellular subsets featuring co-expression with Ecad, ABCB5, SOX4, BZW2 or TAP1 and median expression of PD-L1^{+} (Figure S14a-d). As previously established immune cells nearly exclusively located to TAP1^{+} areas (Figure S14c, d).

On the molecular and single cell level, SOX4 expression clearly discriminated MET^{+} subsets (Figures S14e, f). MET activation (Figure S14g) likely provides growth and cell survival benefits to tumor cells. We observed that melanoma patients with low levels of MET, SOX4 and BZW2 showed most favorable outcome while the combination of MET^{high}/BZW2^{high},

MET^{high}/SOX4^{high} and BZW2^{high}/SOX4^{high} was associated with worst survival probability (Figures S14h-j).

The de-differentiation of melanoma is linked with stemness and expression of NGFR[18,55], however the cellular features of de-differentiated NGFR^{+} tumor cell states are not well characterized. In contrast to the Pat15 specimen, which featured immune cell infiltration despite expression of NGFR, the tumors showed Ecad^{+} areas, i.e. a rather differentiated than de-differentiated phenotype. This was particularly evident in Pat 23 specimen, associated with high expression of NGFR (Figures S15a, b). We observed up to ten cellular subsets and validated the co-existence of proliferating/cycling (TOP2A^{+}) and dormant/non-cycling populations of NGFR^{+} cells, suggesting distinct responses. Cellular subsets additionally featured expression of LIFR (leukemia inhibitory factor receptor), LOX (lysyl-oxygenase) and AXL (AXL receptor tyrosine kinase). Furthermore, we confirmed a poorly understood correlation between NGFR and TRIL identified in our previous study[19]. The more detailed marker analysis of sub clusters revealed additional characteristics of NGFR^{+} cells such as association with SRY-box transcription factors such as SOX4[56], SOX9[57] and SOX11[58] (Figure S15e), transcription factors that are known to promote dedifferentiation.

The expression of NGFR in melanoma has been associated with stemness, cell migration, drug resistance and immune suppression. However, the progressive phenotype of NGFR^{+} cells and patients' outcome seem to be highly dependent on the effects of associated and co-expressed genes. While the exact mechanisms of activation of NGFR in solid cancers, particularly melanoma, remains elusive, several lines of evidence suggest a connection between APP (Amyloid Beta Precursor Protein) and NGFR activation mediated NGF (Nerve Growth Factor). We observed APP expression in close proximity to NGFR-positive cells in a subset of tumors (Figure S15f). NGFR expression was associated with poorer survival, particularly in tumors with co-expression of APP or SOX4. Most intriguingly, we found distinct and co-expression of NGFR and AXL showing different levels of patient outcomes. Our spatial transcriptomics approach validated most genes of the previously identified NGFR

signature and revealed heterogeneity of NGFR^{+} subgroups that could define distinct routes of tumor progression.

Relapse under BRAFi is accompanied by changes in the cellular composition of tumors

The reactivation of the MAPK pathway drives relapse under BRAFi therapy and cross-resistance to ICi[55], hence establishing an immune-evasive tumor microenvironment. Changes in cellular architecture of tumors are likely to be associated with the selection of resistant subclones, resulting in minimal residual intracranial disease (MRID) and relapse. To decipher the cellular compositional changes potentially associated with MRID, we performed spatial profiling followed by unbiased clustering and post Xenium H&E alignment (see STAR Methods) of a BRAFi/MEKi (Tafinlar/MEKinist)-sensitive/naïve (pre-relapse) MBM located in the cerebellum of a cancer of unknown primary (CUP) patient (Figure 5a). The MBM which developed under BRAFi/MEKi therapy in the frontal lobe was observed and resected ~5 weeks after treatment initiation. Reactivation of MAPK signal transduction was confirmed by phosphorylation of ERK1/2 (pERK1/2$^{Thr202/Tyr204}$) in pre- and post-relapse MBM, which was focused on defined microdomains/niches rather than extending throughout the tumor (Figure S16a, b).

Initial comparative spatial mapping and marker analysis of cell clusters revealed significant differences in the composition and architecture of concordant, metachronous tumors during progression (Figure 5b, c and Figure S15c), while TargetSeq of tumors showed low genetic variability and maintenance of the proportion of BRAF^{V600E}-mutant cells (Figure 5b, Figure S15d), which suggests an evolutionary connection between the tumors. Particularly, we observed significant higher levels of CD8A^{+} T cells and C1QC^{+} TAMs and enrichment of a tumor cell cluster (TC_5) which comprised subsets showing expression of inhibitors of insulin signaling IGFBP3 and IGFBP5 (Figure 5c, Table S2) in the BRAFi resistant, frontal lobe MBM. Moreover, we observed enrichment or compositional changes of cell clusters, particularly cycling TCs_3 during relapse, suggesting that progression accompanied

exclusion of potentially dispensable cells or was associated with changes in cell states such as differentiation or de-differentiation. In line with previous reports, we found cycling cells expressing TOP2A, PCNA, CENPF and MET as most persistent subsets[59,60].

Considering that BZW2 or SOX4 serve as potential suppressors of immune cell infiltration that control disease progression by facilitating tumor cells to evade immune recognition, we aimed to investigate whether BZW2- and/or SOX4-associated programs can determine the extent of immune cell infiltration and thus drive MRID. In line with our previous observations, the inverse correlation of TAP1 and potential marker of immune suppression we observed low levels of SOX4 and BZW2 in the post-relapse tumor featuring spatially-defined immune scores and high expression of TAP1 (Figure 5d). Immune scores reflected the spatial distribution of areas of high and low levels of enrichment of immune (T) cells and TAMs (Figure 5d, right panels). We performed in-depth analysis of cellular subsets of niches at immune score-enriched areas and observed predominant enrichment of $TAP1^{+}/CD8A^{+}/TRAC^{+}$ cells at the edge of the tumor at the transition to the microenvironment (Figures 5e, f). On the single cell transcript level, we observed distinct and co-expression of TRAC and TAP1, suggesting T cell heterogeneity (Figure 5f, right panel). Our data therefore suggest that evolutionarily related tumors can nevertheless form different ecosystems that show different levels of immune cell infiltration, determining the response to BRAFi/ICi.

IGF binding proteins (IGFBPs) bind to IGF-1 and block IGF-1/PI3K signaling, which in turn mediates resistance to BRAFi expression. Association of their expression patterns with patient outcome is complex and conflicting evidence suggests supportive and inhibitory functions of tumor progression[61,62]. We observed spatially defined areas of IGFBP3 expression predominantly in the resistant/relapsed tumor (Figure S15e) which was accompanied by co-expression of IGFBP5 and LOX and reduction of Ecad/CDH1 (Figures S15f, g). However, distinct and co-expression of both IGFBPs may induce different effects. Although the role of IGFBPs in melanoma seems to be double-edged, increased expression of IGFBP5 was linked to poor outcome in breast cancer patients[62]. We investigated the levels

of IGFBP3 and IGFBP5 in A375 cells after vemurafenib (Vem) treatment with and without combination of MEK inhibitors cobimetinib (Cobi) or trametinib (Tram). The selection of cells for drug resistance was accompanied by increased levels of IGFBP3 following treatment with Vem+Tram or increased levels of IGFBP5 in cells with acquired resistance to Vem+Cobi or Vem+Tram (Figure S16h). This may hence point out to a potential role of both IGF binding proteins mediating resistance to BRAF inhibitor therapies.

STAR Methods

Patient samples

All procedures performed in this study were in accordance with the ethical standards of the respective institutional research committees and with the 1964 Helsinki Declaration and its later amendments or comparable ethical standards. All patients gave written informed consent for the collection and scientific use of tumor material which was collected at the Department of Neuropathology, Charité-Universitätsmedizin Berlin, Germany and Department of Pathology, Universitätsmedizin Greifswald, Greifswald, Germany. The usage of archived (FFPE) melanoma and central nervous system-derived control samples has been reviewed and approved by the Ethics Committee of the Charité (EA1/107/17 and EA1/075/19) and Universitätsmedizin Greifswald (BB 001/23).

Tissue microarray (TMA)

Hematoxylin and eosin (H&E)-stained brain metastasis tissue sections were examined to identify morphologically representative regions for inclusion in the tissue microarray (TMA) block. For each case, one to three tumor areas were selected under a conventional microscope (Nikon Eclipse Ni-U, Düsseldorf, Germany). Selected regions were marked on the slides and matched to the corresponding donor blocks. TMA construction was performed using a Manual Tissue Arrayer Model I (MTA-1; Estigen OÜ, Tartu, Estonia). A blank paraffin recipient block was first prepared, and cylindrical holes (1.5 mm diameter) were punched into

it. Tissue cores of the same diameter were then extracted from the marked regions of the donor blocks and transferred into the recipient block, resulting in a TMA block containing 14 tissue cores (see graphical abstract, Figure 1). The completed TMA block was incubated at 60 °C for approximately 20 minutes to fuse the tissue cores with the paraffin. Finally, the block was sectioned and stained for downstream analysis.

DNA extraction and quantification

DNA was extracted from FFPE tissue using the Promega® RSC DNA FFPE Kit. Samples were pretreated with 300 µL mineral oil at 80 °C for 2 minutes, followed by lysis with proteinase K for 30 minutes at 56 °C. Extraction and quantification were performed automatically using the Maxwell® RSC instrument (AS4500) and Quantus fluorometer (QuantiFluor ONE dsDNA, Promega, USA).

Genetic Profiling of MBM using TruSight Oncology 500 (TSO500)

Library preparation followed the manufacturer's protocol (Illumina, USA). Briefly, 100 ng DNA was sonicated using a Covaris ME220 sonicator (settings per Illumina, Table S1) to yield fragments averaging 245 bp, confirmed via TapeStation 4150 (Agilent, USA). After end-repair and A-tailing, adapters with unique molecular identifiers (UMIs) were ligated, followed by index PCR. Target enrichment involved two hybridization steps with biotin-linked probes, captured using streptavidin magnetic beads, and amplified by PCR. Libraries were bead-normalized, pooled, denatured, diluted, and sequenced on an Illumina NextSeq 550 DX (2×101 bp paired-end, dual index). Base call files (bcl) were processed using Illumina DRAGEN TruSight Oncology 500 Analysis Software v2.5.3 for FASTQ generation, alignment to hg19, variant calling, and QC evaluation (Q30, coverage >100×, contamination). All metrics met Illumina specifications. Variants from DRAGEN were further annotated via MyVariant.info's REST API, queried with the MyVariant Python module. Variants considered included exonic SNVs, indels, splice mutations, and clinically relevant entries (ClinVar). Polymorphisms were excluded based on the 1000 Genomes project, with a mutation allele frequency threshold of 5%. Benign and likely benign variants were excluded from reporting.

Methylome profiling (EPICv2 Array)

For global methylome analysis, 100-250 ng genomic DNA were subjected to bisulfite conversion using the EZ DNA Methylation-Gold Kit (Zymo Research) according to the manufacturer's protocol. Subsequently, samples were analyzed on the Infinium MethylationEPICv2 Kit (Illumina) according to the manufacturer's recommendations to obtain genome-wide data from 950,000 CpG positions. Raw data from Illumina Epic arrays were preprocessed and analyzed in the standard workflow of the packages RnBeads[63] and watermelon[64] and CNV profiles were calculated using the conumee package[65].

Panel design

The panel was designed as previously described. Panel genes are shown Table S9.

Spatial transcriptomics analysis

Xenium in situ analysis (10X Genomics) was performed with the human brain base panel (hBrain_v1, 266 genes) together with a 100 gene custom add-on panel. TMA and whole tumor sections were prepared and processed according to manufacturer's guidelines (CG000578, Rev D; CG000760, Rev A). Briefly, the sections underwent sequential deparaffinization and permeabilization, followed by overnight hybridization with custom probes at 50°C, rolling circle amplification, and slide-read out in the Xenium Analyzer. After run completion, H&E staining were performed following Xenium guidelines (CG000613, B).

Processing and analysis of data

Spatial analysis of the Xenium readouts of TMA and MBM samples were analyzed using the VoltRon (version 0.2.0) R package[30]. Individual TMA cores were interactively separated into distinct samples using the *subset(object, interactive = TRUE)* function. TMA cores were grouped into patient/donor of origin prior to downstream analysis. Cells with transcript counts less than 5 were removed prior to clustering. Prior to clustering and cell type annotation, post Xenium H&E images of TMA cores and remaining samples were automatically aligned to DAPI channels of the Xenium data stored in the associated VoltRon objects using the *registerSpatialData* function. Seurat (version 5) package[66] was used to perform downstream

unbiased clustering of Xenium cells from both TMA cores and the remaining MBM samples. Log normalized counts (*NormalizeData* function) was performed with a scaling factor = 100. This is followed by dimensionality reduction with PCA and UMAP, and then clustering with shared nearest neighbor graphs (*FindNeighbors* and *FindClusters* function) using parameters specific for each sample. UMAP of Xenium cells across all TMAs were calculated using Harmony-based[67] integrated PCA embeddings of all TMAs. Marker analysis was performed to detect differentially expressed (DE) genes specific to each cell cluster (*FindAllMarkers* function). Cell types were annotated using a hybrid approach, specifically by **(i)** investigating DE genes and **(ii)** interactively visualizing clustered cells and aligned H&E images using TissUUmaps tool[68]. VoltRon objects were converted into anndata (h5ad) format prior to interactive visualization using the *as.AnnData* function. We used the AddModuleScore function from Seurat to calculate the immune module scores using a predetermined set of genes. Cells associated with hot and cold regions, which are areas of around the cells with high immune score were automatically detected via hot spot analysis utilities available in VoltRon. We first constructed a spatial neighborhood graph to identify pairs of cells within 40 or 50 pixel distances (*getSpatialNeighbors* function), and tested significant local changes in the immune score for each cell using Getis-Ord[31] statistics. To detect significant changes of gene expression across hot and cold regions we aggregated the count of cells annotated as hot and cold, and then performed DE analysis with the DESeq2 R package[69]. Aggregation was performed across (i) tumor cells and cells of the TME or (ii) only tumor cells depending on the genes whose expression were compared across hot and cold niches (Table S4).

Immunohistochemistry

Automated immunohistochemical staining of formalin-fixed, paraffin-embedded (FFPE) tissue sections (2 µm thick) was performed on a VENTANA Benchmark XT automated staining instrument (Ventana Medical Systems, Tucson, AZ) according to the manufacturer's instructions. The primary and secondary antibodies used are listed in the STAR Methods section. Slides were deparaffinized using EZ Prep solution for 30 minutes at 75 °C. Antigen

retrieval was performed on the automated stainer using CC1 solution for 60 minutes at 95 °C. Primary antibodies were then applied and visualized with either the iVIEW DAB Detection Kit or the ultraView Universal Alkaline Phosphatase Red Detection Kit (Ventana Medical Systems). All slides were counterstained with hematoxylin for 8 minutes. Immunohistochemical results were independently evaluated by two consultants in neuropathology and pathology based on predominant staining intensity. Omission of the primary antibodies, as a control for nonspecific secondary antibody binding, resulted in absence of labeling. For validation, positive control tissues - fixed and processed in the same manner as the test sections and known to contain the target molecule (e.g., colon carcinoma) - were included in each staining run.

MET-FISH analysis

MET-FISH for evaluation of MET amplification was performed as previously described[70].

Discussion

The tumor ecosystem is defined by spatial interactions between the tumor and environmental cells and is presumably altered over time due to intrinsic factors such as mutations or gene amplifications that drive subclonal evolution[71]. On the other hand, tissue-resident cells such as cancer-associated fibroblasts (CAFs) or endothelial cells which together with the extracellular matrix form the tumor bed. The ecosystem of brain metastases comprises cells located specifically in the brain including astrocytes, oligodendrocytes, microglia and neurons besides immune cells and macrophages which infiltrate the brain in response to neuro-inflammatory processes[72]. Brain infiltrating tumor cells and neuro-degenerative diseases such as Alzheimer and Stroke or Ischemia presents main determinants of neuro-inflammation, mediated by activated astrocytes and microglia[73]. The multitude of interactions between environmental cells in their ground state, i.e., in a non-activated state, and tumor cells is in itself a complex process that probably defines the early stages of asymptomatic

brain metastasis. The complexity of this still not entirely understood system increases in a time-depended manner, suggesting different types of ecosystems (ground state/moderately inflamed and highly inflamed) which in turn distinctly respond to therapeutic interactions.

Spatial transcriptomics-based profiling provided insights into the different stages of MBM

Our spatial transcriptomics approach provides for the first time insights into the spatial maps of MBM of different clinical stages, considering the NGFR^{+} tumor stage representing a rather resistant, de-differentiated/ stem-like phenotype and the Ecad^{+} subset of melanotic /pigmented MBM featuring therapy-naïve or responsive phenotypes. De-differentiation in general considerately forces tumor cell stemness and increasing tumor heterogeneity and drives immune evasion and resistance to immunotherapy[18,74], suggesting NGFR expression in melanoma as potential biomarker of ICi response. However, our approach revealed remarkable heterogeneity in the NGFR^{+} cell fraction and suggests that factors potentially interacting with NGFR define the phenotypes of NGFR^{+} tumor cells. Our approach confirmed coexisting and intermediate states and demonstrated the validity of our previously identified signature genes that classify Ecad/NGFR states. Although we found BZW2 and SOX4 among the most downregulated genes in BMCs with knockdown of NGFR, our spatial data suggest no direct regulatory association of NGFR and SOX4 or BZW2 but suggest a broader function MBM. Bulk[19] and single-cell RNAseq MBM[75] studies revealed potential cellular subgroups but only the integration of spatial information revealed the distribution of immunologically cold, BZW2^{+}, and/or SOX4^{+} and TAP1^{+} areas with immune cell infiltration in the tumors. TAP1 serves as important antigen transporter in tumor cells and immune cells ensuring the presentation of antigens to T cells via MHC class I molecules. We initially observed this clear distinction between immune cell-enriched and depleted regions, which correlated with the expression of TAP1/BZW2, by spatial transcriptomics profiling and mapping to H&E of a primary mucosal melanoma. We found these regional differences in the associated MBM, suggesting that primarily the BZW2^{+}/TAP1^{low} tumor cells escaping immune

surveillance are prone to metastasis or that immunosuppressive areas are re-established during the development of MBM, possibly in response to therapeutic interventions. On single cell-level we observed tumor cells with high abundance of either BZW2 or TAP1 transcripts as well as intermediate cells with moderate levels of both, however only the $BZW2^{low}/TAP1^{high}$ tumors were associated with favored survival of melanoma patients. Moreover, we confirmed the relationship of BZW2 and TAP1 in additional tumor samples but observed overlapping patterns of BZW2 and SOX4 acting in concert or in a substituting manner.

Mechanistically, the direct regulation of NGFR and of the BZW2/AP1-axis in melanoma remains elusive. SOX4 serves as a downstream target and mediator of epithelial-mesenchymal transition (EMT) of TGFβ signaling in breast cancer[76] but this connection was not particularly visible spatially. The competitive inhibitor of eukaryotic translation initiation factor 5 (eIF5) BZW2 which represses translation starting at non-canonical start codons[77] was potentially linked with mTOR signaling and associated with a pro-tumorigenic phenotype in several cancers[78]. The regulation of TAP1 and of additional genes involved in the MHC class I antigen-presentation pathway depends on interferon signaling[39,41,79] and on the key transcriptional coactivator NLRC5[80] which is often silenced by promoter methylation[80]. However, additional studies will be required to uncover the regulation of immune suppressive niches which can be defined not only by $BZW2^{+}$. The automated profiling of “cold” and “hot” niches using hot spot analysis, as predefined by the degree of immune cell infiltration uncovered a spatial signature of markers of $TAP1^{+}$ niches. Niches comprised $TAP1^{+}$ tumor cells and immune cells among other marker-defining cell types, particularly immune cells (CCL4, ITGB2, LGALS9), TAMs (C1QC, FCER1G, AIF1) and niche forming tumor cells (TAP1, HLA-DRA).

A 10-gene IFNγ signature was identified that includes STAT1 and HLA-DRA among others and predicts the response to ICi therapy[81]. In line, we observed “hot” niches associated with IFN cells which showed high levels of mediators of interferon signaling such as MX1 or IFI6

and found STAT1 and HLA-DR(A) proteins expressed at sites of low BZW2/SOX4. Although the circumstances of BZW2 regulation remains elusive, we assume that BZW2+ cells exhibit erroneous STAT1 expression and activation which in turn is responsible for low TAP1 levels and impaired antigen presentation and immune (T) cell attraction.

In summary, we have identified a significant role for BZW2 and TAP1 as inversely correlated tumor markers that correspond to a high or low degree of immune infiltration and spatially separate tumors by yet undefined mechanisms. Therefore, the BZW2/TAP1 system could serve as an additional level of immune regulation alongside the therapeutically important PD1/PD-L1 axis.

Spatial profiling uncovered the cellular heterogeneity of tumors

Besides spatial mapping and characterization of immune niches, our approach provided insights into the cellular composition of tumors and demonstrated an impressive heterogeneity of tumor cellular subsets. We observed that progression was accompanied by enrichment and depletion of cellular subsets, suggesting a restructuring of the tumor ecosystem. The comparative spatial mapping, analysis of genetic and copy number profiles uncovered MET receptor as a potential driver of brain metastatic progression. We found MET receptor amplification in methylome-based CNV profiles of the mucosal melanoma-derived MBM and loss of the driver mutation $NRAS^{Q61}$ as a potential sign of resistance and progression[82]. Examination of the MET+ cell fraction revealed at least five cellular subgroups that co-expressed Ecad, ABCB5, BZW2, and SOX4 or showed MET phosphorylation/activation. The large diversity of MET^{+} subsets suggests that small molecule MET inhibitors could eliminate immunosuppressive $BZW2^{+}/SOX4^{+}$ subsets, making them a promising second-line treatment strategy for BRAFi/ICi-resistant primary and (brain) metastatic melanoma. As MET receptor serves as mediator of BRAFi resistance, the combination of MET inhibitors potentially increase efficacy of ICi in BRAFi refractory tumors.

Besides MET, our survey allowed the sub-classification of the NGFR tumor cell fraction which underscores that NGFR$^+$ cells feature functional diversity depending on the co-expressed and in concert acting genes.

The relevance of exploring NGFR$^+$ tumor cells in melanoma and other tumor entities such as glioblastoma has already been convincingly demonstrated by our own work and that of other groups. We can therefore assume that there are several cellular and possibly interconnected subgroups of e.g. MET and NGFR that determine the properties and therapeutic response of tumors depending on the context. Spatial transcriptomics paves the way for understanding the biology of these subgroups and how we can use them for therapeutic purposes.

Data Availability

A TissUUmaps-based interactive application of annotated Xenium cells and aligned post-Xenium H&E images of all MBM samples are publicly available at https://brain-melanoma-tissuumaps.mdc-berlin.de/ . All spatial transcriptomics raw data are deposited at GEO (Gene Expression Omnibus; study GSE306955). For integrative analyses our study included bulk expression data of MBM (study EGAS00001005975 (https://zenodo.org/record/7013097) and of melanoma prior and after ICi therapy (study by Liu et al.) and single cell expression data of candidates BZW2, SOX4 and PD1/PD-L1 of melanoma showing response or resistance to immune checkpoint inhibition (study GSE115978); https://portals.broadinstitute.org/single_cell/study/melanoma-immunotherapy-resistance) and therapy-naïve MBM (study GSE200218). For assessment of the potential role of IGFBPs 3/5 in drug resistance, we investigated A375 cells with acquired resistance to BRAFi/MEKi (study GSE164897).

Code Availability

The R scripts used to analyze TMA and MBM samples as well as scripts to generate the figures are available at https://github.com/LandthalerLab/MBM_Analysis_Manukyan.

Figure legends

Figure 1: Graphical abstract. For initial assessment and later analyses, single cell and bulk RNAseq studies were used as summarized on the left site. We used Xenium 10X technology for single cell-resolved spatial transcriptome profiling of MBM (n=14) including adjacent CNS samples (n=2) and PCNSL (n=2) compiled in a TMA (1) and whole MBM sections (not shown). Following processing and data analysis, molecular profiling unraveled molecular subtypes Ecadhigh, NGFRhigh/de-differentiated or the immune suppressive subgroups BZW2high and/or SOX4high (2). Our study uncovered TAP1 and BZW2/SOX4 as niche-determining factors and potential prognostic markers of melanoma survival (3).

Figure 2: BZW2 and TAP1 distinct spatially separated areas of immune cell infiltration. a.) Left panel: UMAP representation of melanoma patients (n=14) showing high (red) or low (blue) level of resistance to immune checkpoint therapy (study GSE115978). Right panel: Levels of BZW2 expression in tumors shown in (a). The expression level is color coded. b.) Box plot representation of levels of BZW2 and SOX4 across single cells of pre-treatment tumors (n=1089 cells) and tumor with acquired resistance (n=792 cells). c.) Box plot representation of tumor (melanoma) samples of patients with complete response (CR), partial response (PR) as well as stable disease (SD) or progressive disease (PD) as best response to nivolumab. d.) Schematic summary of disease progression of Pat 90 who was first diagnosed with mucosal melanoma in the nasal cavity (09/2021). Lung metastases showed response to applied ICi (09/2022-02/2023). Emerged MBM was resected (06/2023), relapse was observed (11/2023). e.) Spatial visualization of areas of $BZW2^+$ cells, proliferating $BZW2^+/TOP2A^+$ cells, $TAP1^+$ cells and immune cells as indicated by colors. f.) TargetSeq of primary mucosal melanoma (mM) and concordant brain metastasis (mMBM) identified missense SNVs/MNVs (single/multiple nucleotide variants) or, duplication (DUP), deletions (DEL) or insertions (INS); not detected (ND) or wildtype (wt) as given by the color code. g.) Spatial representation of expression levels of BZW2 and TAP1 in primary mM and

mMBM showing discrete areas of BZW2$^+$ or TAP1$^+$ tumor cells upper, center panels. Indicated H&E areas show immune-cell enriched areas (lower panels). h.) Visualization of spatially-defined immune scores (ImmuneScores) in indicated tumors. i.) Illustration of automatically detected (hot spot analysis) immunogenic “hot” (yellow) and suppressive “cold” (blue) areas within a represented set of tumors. j.) Box plots showing levels of selected representative markers for “hot” niches: TAP1, HLA-DRA, PD-L2 (PDCD1LG2) and ITGB2 (upper row) and “cold” niches: BZW2, PSENEN, SOX4 and SOX6 (lower row) as determined by DESeq2 analysis. All markers were significantly differentially expressed between “hot” and “cold” areas across all aggregated niche-building tumor cells of selected aggregated tumor samples (TMA and non-TMA). Box and whisker plots show median (center line), the upper and lower quartiles (the box), and the range of the data (the whiskers), including outliers. k.) reconstruction of an immunogenic niche, containing immune (T) cells (pink) and TAMs (light pink) which are surrounded by TAP1$^+$ “hot” tumor cells (TCs, greenish brown). The immunogenic niche in turn is embedded in the suppressive area by BZW2$^+$ cells (blue) and intermediate cells (color gradient). Lower scheme: enlarged illustration of cells indicated above indicting the distances of TAP1$^+$ and BZW2$^+$ cells to nearest immune cells. l.) Violin plot indicating the distances of immunogenic and suppressive tumor cells to nearest immune cells as calculated across n=61,071 TAP1$^+$ and n=146,947 BZW2$^+$ TCs. In b, c significance was determined by unpaired t-test, in (j) significance was determined by DESeq2 analysis. m.) Transcript abundance and localization of TRAC, TAP1 and BZW2 (left panels) or CD8A, TAP1 and HLA-DRA (right panels) in single cells of indicated (microscope symbols) sites of investigation of primary mM shown in (g). The mutually exclusivity of BZW2 and TAP1 and association of TAP1 with HLA-DRA and CD8A is shown. n.) Transcript abundance and localization of TRAC, TAP1 and BZW2 validating distinct immune suppressive (BZW2$^+$) and T cell infiltrated (TRAC$^+$), immune supportive (TAP1$^+$) areas. Endothelial cells are indicated by PECAM1.

Figure 3: Spatial and single cell profiling identified interferon signaling as a component of immune cell-enriched niches. a.) Simplified scheme showing the principal

composition of immune cell-enriched niches. Tumor cells with high BZW2 levels surround $TAP1^+$ cells, which in turn form the bed of immune cells. b.) Survival probability of melanoma patients (TCGA-SKCM, n=459) featuring high or low levels of BZW2 and TAP1. Cox-regression analysis revealed significant (Logrank P = $7.3x10^{-7}$) dependence of overall survival (OS) on BZW2 (HR=1.355) and TAP1 (HR=0.485). c.) Pattern of expression of BZW2 and TAP1 in single (Malignant) tumor cells of therapy-naïve MBM (study GSE200218). Expression is color coded. d.) Illustration of the top MBM expressed TAP1-associated genes demonstrating enrichment of mediators of interferon (IFN) signaling (STAt1, IFI6), immune proteasomes (PSMB8/9) and mediators of antigen transport and presentation (HLAs A/C/E) and TAP2. e.) Box plot representation of expression levels of MX1 and LGALS9 calculated across tumor cells and TME cells which represent the immune cell enriched ("hot") niches. Significance was determined by a unpaired two-tailed, t-test. Box and whisker plots show median (center line), the upper and lower quartiles (the box), and the range of the data (the whiskers), including outliers. f.) Simplified scheme illustrating some key players of interferon signaling, highlighting the most important IFN-regulated genes. g.-f.) Spatial mapping of IFI6 (Interferon Alpha Inducible Protein 6) revealed hot spots in $TAP1^+$ areas in Pat90 mM and MBM (first panels). Characterization of major cell types within $IFI6^+$ primary and secondary immune niches unveiled T cells ($TRAC^+$) surrounded by $TAP1^+/IFN^+$ tumor cells (TCs). i.) Left panel: Composite illustration of $STAT1^+$ cells. Center panels: IHC of Pat 90 tumors for STAT1. Right panel: Spatial neighborhood of MET^+ cells.

Figure 4: Spatial profiling uncovered distinct and common molecular subgroups across multiple tumors. a.) Upper scheme: indicating the localization of TMA tumors (MBM, PCNSL) and adjacent-normal CNS tissue at primary (nasal cavity, Pat 90) or intracranial sites as indicated. Lower scheme: representation of proportions of major cell types indicating the cellular heterogeneity of TMA samples. b.) UMAP of defined major cell types of TMA samples revealed marker-based identification of tumor cell (TC) subsets and TME cells as illustrated. c.) Heat map showing the top expressed markers of cellular, color coded subsets shown in (b). d.) Spatial maps illustrating the expression of BZW2, SOX4, and NGFR in

tumor samples, sorted by immune score (IS). e.) UMAP representation of IS and expression of BZW2 and TAP1, discriminating cellular subsets/tumor subtypes. The level of expression is color coded. f.) Single cell spatial resolution of a $TAP1^+$ niche of an immune-depleted MBM (Pat 23-P, punch C). g.) Abundance of transcripts of BZW2, TAP1, CD8A and CTLA4 (upper panels) or TAP1, CD8A and HLA-DRA (lower panels) of the $TAP1^+$ niche shown in (f) h.) Single cell spatial resolution of a $TAP1^+$ niche of Pat 90 mM, showing transcripts of TAP1 (red), CD8A (green), HLA-DRA (purple) and BZW2 (blue).

Figure 5: Low immune cell content fosters relapse and accompanies changes in the cellular architecture of the tumor´s ecosystem. a.) Schematic representation of disease progression starting from initial diagnosis 07/2015 and resection (08/2015) of a cerebellar MBM of a CUP patient (Pat 19). The MBM which emerged under BRAFi/MEKi therapy was resected ~5 weeks after initiation of the therapy. b.) Comparative spatial mapping of major cell types revealed changes in the tumor ecosystems. c.) Left panel: Proportions of indicated, color coded major cell types characterizing MBM. Right panel: Heat map showing normalized expression of top expressed markers in cellular subsets. d.) Spatial maps indicating localization and level of expression of BZW2, SOX4, TAP1 and immune scores in post-relapse (upper row) and pre-relapse (lower row) tumors. e.) Single cell representation of areas of investigation as indicated (microscope symbol) in (d) showing major cell types. f.) Left panel: Illustration of the spatial context of T cells ($CD8A^+$) at the tumor ($TAP1^+$)-stroma (DCN^+) cell crossing. Right panel: Abundance of transcripts of tumor cell expressed SOX4, TAP1, MET and ABCB5 or immune cell expressed markers TRAC and TAP1. Magnified area shows a T cell niche. g.) Single cell representation of the major cell types of an immune cell niche in mMBM. h.) Left panel: Spatial mapping of $SOX4^+$ and $TAP1^+$ cells. Right panel: Abundance of transcripts of tumor cell expressed SOX4, TAP1 and ABCB5 or immune cell expressed markers TRAC and TAP1.

Figure S1: BZW2 and SOX4 serve as potent immune suppressors in MBM. a.) Intersection of genes expressed in MBM but not BC (n=530) and IRP (immune resistance

program, n=302) genes identified BZW2 and SOX4. b.) GSEA of bulk expression data from MBM and BC samples for enrichment of IRP genes and genes characterizing the ICi-responsive status in MBM with suppression of IRP. c.) Box plot representation of levels of BZW2, SOX4 and CDK4 in brain controls (BC), MBM-derived cell lines (BMC) and MBM. d.) UMAP representation of SOX4 expression in tumor cells of melanoma patients (n=14, study GSE115978). The expression level is color coded. e.) Left panel: UMAP representation of illustrating the PD1/PD-L1 status of patients in (d), center and right panels: Violin plots indicating the expression levels of BZW2 and SOX4 in $PD1^{pos}$, $PDL1^{pos}$ or $PDL1^{neg}$ tumor cells. f.) Box plot representation of levels of TAP1 and HLA-DRA across single cells of pre-treatment tumors (n=1089 cells) and tumor with acquired resistance (n=792 cells). g.) Survival probability of melanoma patients (TCGA-SKCM, n=459) featuring high or low levels of BZW2 (left panel), SOX4 (center panel) and TAP1 (right panel). Cox-regression analysis revealed significant (Logrank $P = 1.1x10^{-3}$; $P = 1.9x10^{-3}$; $P = 4.4x10^{-6}$;) dependence of overall survival (OS) on BZW2 (HR=1.550), SOX4 (HR=1.520) and TAP1 (HR=0.450). In b, d significance was determined by a unpaired two-tailed, t-test. Box and whisker plots show median (center line), the upper and lower quartiles (the box), and the range of the data (the whiskers), including outliers.

Figure S2: Comparative spatial profiling revealed patterns of brain metastatic progression. a.) Spatial mapping of disease progression of primary mucosal melanoma (primary mM, initially diagnosed 09/21) to the brain (mMBM, resected 06/23) indicating pronounced changed in the tumor ecosystems with particular focus on tumor cell subsets 4 (TCs_4, $TAP1^{+}$) and TCs_7/8 ($SLC17A6^{+}$). b.) Comparative UMAP indicating the enrichment, depletion and overlapping of cellular subtypes which accompanied metastatic disease progression. Cellular subsets are color coded. c.) Heat map representing the top expressed markers in cellular subsets indicated in (a-b). Important cellular subsets are highlighted. d.) Left panel: Proportions of indicated, color coded major cell types characterizing the indicated tumors. Right panel: Stacked bar plot shows levels of BZW2 and TAP1 in indicated tumors.

e.) Comparative UMAPs indicating levels of BZW2 (first panel), TAP1 (center panel) and SOX4 (right panel). The expression level is color coded.

Figure S3: Profiling revealed characteristics of immunogenic "hot" and suppressive "cold" niches. a.) Single spatial mapping of BZW2 expression of immune scores (first and second row) and composite visualization of BZW2 and immune scores (third row). Automated detection and assignment of immune niches using hot spot analysis (fourth row) and of niche-supporting "hot" tumor cells (fifth row). Expression levels and cellular subsets are color coded. b.) Box plot representation of expression levels calculated across all niche-encompassing tumor and TME cells of selected aggregated tumor samples (TMA and non-TMA). Immune cell markers NKG7 (natural killer cells), CCL5, CD8A (both T cells), C1QC (TAMs) were significantly enriched in "hot" niches. Levels of tumor cell markers MET and IGFBP3 were calculated across all niche-building aggregated tumor cells. Box and whisker plots show median (center line), the upper and lower quartiles (the box), and the range of the data (the whiskers), including outliers. In b significance was determined by significance was determined by DESeq2 analysis, corrected for multiple testing.

Figure S4: Methylome-based CNV analysis revealed amplification of MET receptor as potential driver of brain metastatic progression. a.) UMAP projection indicating the changes in immune scores (upper panel) and levels of CD8A expression (lower panel) in Pat 90 tumors (primary mM; MBM). Levels are color coded. b.) Illustration of chromosome-wide copy number changes, genes on chromosome (Chr.) 7, particularly MET are highlighted. c.) Upper panels: MET-FISH analysis of tumors shown in (a) revealed amplification of genes on chromosome 7 (CEN7 probe, red) such as MET (MET-specific probe, green). Lower panel: Box plots representing probe-specific counts of fluorescent signals of investigated DAPI-stained nuclei (n=50) in depicted tumor sample.

Figure S5: Levels of STAT1 and BZW2 determine survival of melanoma patients. a.) Survival probability of melanoma patients (TCGA-SKCM, n=459) featuring high or low levels of BZW2 (left panel) and HLA-DRA. Cox-regression analysis revealed significant (Logrank P

= $6.1x10^{-9}$) dependence of overall survival (OS) on BZW2 (HR=1.297) and HLA-DRA (HR=0.462). b.) Survival probability of melanoma patients with MBM (study EGAD00001005046, n=74) featuring high or low levels of TAP1. Cox-regression analysis revealed significant (Logrank P = $6.3x10^{-4}$) dependence of overall survival (OS) on TAP1 (HR=0.420). c.) Malignant and non-malignant cells of therapy-naïve MBM (study GSE200218) are shown as indicated. d.) Survival probability of melanoma patients (TCGA-SKCM, n=459) featuring high or low levels of BZW2 (left panel) and STAT1. Cox-regression analysis revealed significant (Logrank P = $1.1x10^{-9}$) dependence of overall survival (OS) on BZW2 (HR=1.403) and STAT1 (HR=0.449). e.) Spatial mapping of expression of SOX4 upper panels) and MET (lower panels) in primary mM and mMBM. f.) Composite representation of $STAT1^+$ cells in the immune cell niche. $STAT1^+$ cells were localized to $TAP1^+$ niches. g.) Spatial mapping of expression of STAT1 in primary mM and mMBM. f.) Composite representation of $STAT1^+$ cells in the immune cell niche. $STAT1^+$ cells were localized to $TAP1^+$ niches. h.) Composite representation of $SOX4^+$ (upper panel) or $PSENEN^+$ (lower panel) cells in the immune cell niche. $SOX4^+$ and $PSENEN^+$ cells were localized to $BZW2^+$ immune “cold” areas in primary MBM.

Figure S6: Profiling of single $TAP1^{high}$ and $TAP1^{low}$ tumor cells revealed a TAP1-associated network. a.) Single cell resolved expression of MET, TAP1 and BZW2. The level of expression is color coded. b.) IHC for HLA-DRA indicating areas of presentation of neoantigens. c.) Network of the top30 identified TAP1-associated genes as analyzed by STRING.

Figure S7: UMAP-based clustering revealed prominent inter-tumor heterogeneity but homogeneity among replicate samples. a.) Table providing information about TMA specimen. b.) UMAP of the unintegrated Xenium cells across all TMAs, illustrating clustering of TMA samples which revealed common and unique cellular subsets. c.) UMAPs of Xenium cells split by individual TMA specimen as indicated by the color code.

Figure S8: Immunohistochemistry classified tumors into for Ecad$^+$ and NGFR$^+$ tumors. a.-b.) IHC for Ecad (red) and NGFR (brown) enabled sub classification of TMA tumor samples (a) and CNS tissue (b).

Figure S9: Immunohistochemistry for MLANA and HMB45 classified tumors into pigmented/differentiated and non-pigmented/de-differentiated. a.-b.) IHC for MART1/ MLANA (a) and HMB45 (b) (indicated by brown staining) enabled sub classification of TMA tumor samples.

Figure S10: Immunohistochemistry for CD3 uncovered immunogenic niches. a.-b.) IHC for CD3 in TMA tumor specimen (a) CNS tissue (b) (indicated by brown staining) provided information about the degree of immune cell infiltration.

Figure S11: Spatial profiling and immunohistochemistry provided insights into inflammatory states of tumor-adjacent CNS tissue. a.-b.) IHC for Iba1/AIF1 in TMA tumor specimen (a) (indicated by brown staining) provided information about the degree of infiltration of tumor-associated macrophages/microglia (TAMs).

Figure S12: Profiling of immune cell niches revealed concomitant IFN signaling. a.) UMAP visualization illustrates the clustering of TMA samples according to donor characteristics. b.) Spatial maps illustrating the expression of MET, ABCB5, and Ecad in samples. c.-e.) UMAP representation of expression of HLA-DRA (c), MET (d) and SOX4 (e), discriminating cellular subsets/tumor subtypes. f.) Investigation of the spatial pattern of expression of BZW2, SOX4, TAP1 (first row) or HLA-DRA, ISG15 and immune scores (second row) or IFI6, IFI44L, PTPRC (third row) or MX2, MX1, CD8A (fourth row) of an immune cell niche in Pat23-P (punch C). g.) Cellular deconvolution and investigation of the spatial pattern of expression of TAP1 (first row), immune scores, BZW2 (second row) or PTPRC, SOX4 (third row) or IFI6, CD8A (fourth row). In (c.-g.) the level of expression is color coded.

Figure S13: Single cell profiling uncovered cellular heterogeneity of immune and tumor cells of immunogenic niches. a.) Abundance of transcripts of BZW2, TAP1, CD8A and HLA-DRA in single cells of an immune niche in Pat90 (primary mM) indicating co-expression of TAP1 and HLA-DRA in tumor cells and in $CD8A^+$ T cells.

Figure S14: Single cell profiling uncovered reactive states of tumor-adjacent astrocytes. a.) H&E staining (upper row) and Iba1/AIF1 of CNS normal_1 indicating areas of TAM activation in distant and adjacent areas of the tumor. b.) Spatial distinct patterns of GFAP expression (first column) in tumor-adjacent, reactive astrocytes (second column) and astrocytes at distant areas (third column). c.) UMAP presentation of major cell types of CNS tissue (a) indicating cellular subsets and different states of astrocytes. d.) UMAP presentation of expression levels of GFAP, CHI3L1, GJA1 (upper row) or MOG, SNAP25, SPP1 (lower row). e.) Spatial representation of cellular subsets in (a) showing enrichment and clear separation of areas of homeostatic (hom.) and reactive (react.) astrocytes and localization of neurons at particularly tumor-distant areas. f.) Spatial representation of expression levels of GFAP, CHI3L1, GJA1 (upper row) or MOG, SNAP25, SPP1 (lower row). g.) Composite presentation of reactive astrocytes ($CHI3L1^+$), neurons ($SNAP25^+$) and oligodendrocytes (MOG^+), (left map) or reactive TAMs (AIF1+), neurons ($SNAP25^+$) and oligodendrocytes (MOG^+) (right map). h.) Bubble plot indicating the top expressed markers in cellular subsets of (a). In c, h, cellular subsets are color coded; in d, f, expression levels are color coded.

Figure S15: BZW2 and SOX4 classify cellular subgroups of MET expressing tumor cells. a.) UMAP-based representation of cellular subsets of Pat 90 (mMBM) indicating tumor cell heterogeneity (TCs) and TME cells. b.) UMAP-based representation of expression levels of MET, Ecad/CDH1, ABCB5 (upper row) or SOX4, BZW2, TAP1 (lower row). c.) Spatial representation of cellular subsets of Pat 90 (mMBM) indicating tumor cell heterogeneity (TCs) and TME cells. d.) Spatial representation of expression levels of MET, Ecad/CDH1, ABCB5 (upper row) or SOX4, BZW2, TAP1 (lower row). e.) Abundance of transcripts of MET, ABCB5, SOX4, BZW2 in single cells (first column) and IHC of pMET and Ecad (second

column) indicating tumor cell subsets defined by expression of SOX4 and activation of MET. f.) Heat map showing expression of top markers of cellular subsets. g.-i.) Survival probability of melanoma patients (TCGA-SKCM, n=459) featuring high or low levels of MET and BZW2 (left panel), MET and SOX4 (center panel) or BZW2 and SOX4. Cox-regression analysis revealed significant (Logrank P = $6.6x10^{-4}$) dependence of overall survival (OS) on MET (HR=1.412) and BZW2 (HR=1.542) and dependence of overall survival on MET (HR=1.372) and SOX4 (HR=1.480), Logrank P = $7.5x10^{-4}$ and dependence of overall survival on BZW2 (HR=1.435) and SOX4 (HR=1.404), Logrank P = $5.1x10^{-4}$.

Figure S16: Single cell spatial profiling uncovered cellular subsets of NGFR^{+} MBM. a.) UMAP-based representation of cellular subsets of Pat 23-P (MBM) indicating tumor cell heterogeneity (TCs) and TME cells. b.) UMAP-based representation of expression levels of NGFR, TRIL, AXL (upper row) or LIFR, TOP2A, LOX (lower row). c.) Spatial representation of cellular subsets of Pat 23-P (MBM) indicating tumor cell heterogeneity (TCs) and TME cells. d.) Spatial representation of expression levels of NGFR, TRIL, AXL (upper row) or LIFR, TOP2A, LOX (lower row). e.) Abundance of transcripts of NGFR, APP in single cells (first column) and IHC of NGFR and APP (second column) indicating tumor cell subsets which are defined by APP-mediated activation of NGFR. f.) Heat map showing expression of top markers of cellular subsets, selected tumor cell subsets are highlighted. g.-i.) Survival probability of melanoma patients (TCGA-SKCM, n=459) featuring high or low levels of NGFR and SOX4 (left panel), NGFR and APP (center panel) or NGFR and AXL. Cox-regression analysis revealed significant (Logrank P = $1.6x10^{-3}$) dependence of overall survival (OS) on NGFR (HR=1.412) and SOX4 (HR=1.542) and dependence of overall survival on NGFR (HR=0.657) and APP (HR=0.790), Logrank P = $5.1x10^{-3}$ and dependence of overall survival on NGFR (HR=0.769) and AXL (HR=0.560), Logrank P = $5.4x10^{-6}$.

Figure S17: Expression of IGFBPs potentially characterize spatially-defined areas of BRAFi resistance in relapsed MBM. a.) Analysis of concordant, metachronous MBM: IHC

for phosphorylated and activated ERK1/2 kinase (pERK1/2$^{Thr202/Tyr204}$) indicating focused areas of activation in the pre-relapse tumor and restored activation in the post relapse tumor. Entire tumor sections (first column), tumor areas which have been selected for spatial transcriptomics investigation and (second column, red dashed line) and magnified areas of ERK activation in pre- and resistant/post-relapse tumors. b.) IHC of TMA samples concordant to punched areas as indicated in entire sections. c.) UMAP presentation of cellular subsets in post-relapse and pre-relapse tumors indicating pronounced compositional changes in cellular subfractions. d.) TargetSeq of primary (pre) and resistant/relapsed (post) MBM identified missense SNVs/MNVs (single/multiple nucleotide variants) or, duplication (DUP), deletions (DEL) or insertions (INS); frameshift variants, inframe deletions, splice donor variants or 3´-UTR variants not detected (ND) or wildtype (wt) as given by the color code. e.) Spatial mapping of IGFBP3 expression indicating discrete sites of IGFBP3 only in the post-relapse tumor. Microscope symbol: areas of investigation. f.) Composite illustration of spatially localized tumor cells within the areas of investigation expressing IGFBP3, IGFBP5 and Ecad/CDH1 as indicated. g.) Abundance of transcripts of IGFBP3, IGFBP5, Ecad and LOX of an areas specific in (f) showing co-localization/co-expression of IGFBP3/IGFBP5 and LOX but mutually exclusivity with Ecad expression. h.) UMAPs representing the single cell subsets and levels of expression of IGFBP3 and IGFBP5 of untreated or vemurafenib (Vem), cobimetinib (Cobi) or trametinib (Tram) treated A375 cells (study GSE164897). Expression levels are color coded.

Acknowledgements

We would like to thank all collaborators, technical staff, and laboratory personnel who contributed to this study. We are especially grateful to Michele Peters, Ayad W.H. Dawood,

Andreas Wendt, Dana Ristau, Katrin Müller, Tanja Propp, Betty Nedow, Jenny Hagemann, and Diana Krüger for their support with sample preparation, immunohistochemistry, sequencing, analysis, and technical assistance. This work was supported by the German Federal Ministry of Education and Research (BMBF): NATON, No. 01KX2121 to H.R. and Seed funding from University Medicine Greifswald to K.P. and by the European Regional Development Fund (EFRE) (Target-H; FV-2024-0022) to JR.

Author Contributions

AM, KP, JR, and TR conceived and designed the study, performed experiments, collected data, analyzed the data, and drafted the manuscript. EW, HR, TC, JA, IP, AA, FR, AL, KK, KJ, and ML performed experiments and provided essential resources. EW contributed substantially to the conceptual development and critical revision of the manuscript. All authors critically revised the manuscript for intellectual content and approved the final version for submission.

References

1. Thomas, F., DeGregori, J., Marusyk, A., Dujon, A.M., Ujvari, B., Capp, J.P., Gatenby, R., and Nedelcu, A.M. (2024). A new perspective on tumor progression: Evolution via selection for function. Evol Med Public Health *12*, 172-177. 10.1093/emph/eoae021.
2. Huang, S. (2013). Genetic and non-genetic instability in tumor progression: link between the fitness landscape and the epigenetic landscape of cancer cells. Cancer Metastasis Rev *32*, 423-448. 10.1007/s10555-013-9435-7.
3. Vogelstein, B., Papadopoulos, N., Velculescu, V.E., Zhou, S., Diaz, L.A., Jr., and Kinzler, K.W. (2013). Cancer genome landscapes. Science *339*, 1546-1558. 10.1126/science.1235122.
4. Brastianos, P.K., Carter, S.L., Santagata, S., Cahill, D.P., Taylor-Weiner, A., Jones, R.T., Van Allen, E.M., Lawrence, M.S., Horowitz, P.M., Cibulskis, K., et al. (2015). Genomic Characterization of Brain Metastases Reveals Branched Evolution and Potential Therapeutic Targets. Cancer Discov *5*, 1164-1177. 10.1158/2159-8290.CD-15-0369.
5. Rigg, E., Wang, J., Xue, Z., Lunavat, T.R., Liu, G., Hoang, T., Parajuli, H., Han, M., Bjerkvig, R., Nazarov, P.V., et al. (2023). Inhibition of extracellular vesicle-derived miR-146a-5p decreases progression of melanoma brain metastasis via Notch pathway dysregulation in astrocytes. J Extracell Vesicles *12*, e12363. 10.1002/jev2.12363.

1079 6. Schroeder, T., Bittrich, P., Kuhne, J.F., Noebel, C., Leischner, H., Fiehler, J., Schroeder, J.,
1080 Schoen, G., and Gellissen, S. (2020). Mapping distribution of brain metastases: does the
1081 primary tumor matter? J Neurooncol *147*, 229-235. 10.1007/s11060-020-03419-6.
1082 7. Redmer, T. (2018). Deciphering mechanisms of brain metastasis in melanoma - the gist of the
1083 matter. Mol Cancer *17*, 106. 10.1186/s12943-018-0854-5.
1084 8. Lau, P.K.H., Feran, B., Smith, L., Lasocki, A., Molania, R., Smith, K., Weppler, A., Angel, C., Kee,
1085 D., Bhave, P., et al. (2021). Melanoma brain metastases that progress on BRAF-MEK
1086 inhibitors demonstrate resistance to ipilimumab-nivolumab that is associated with the Innate
1087 PD-1 Resistance Signature (IPRES). J Immunother Cancer *9*. 10.1136/jitc-2021-002995.
1088 9. Serra, E., Abarzua-Araya, Á., Arance, A., Martin-Huertas, R., Aya, F., Olondo, M.L., Rizo-Potau,
1089 D., Malvehy, J., Puig, S., Carrera, C., and Podlipnik, S. (2024). Predictive and Prognostic
1090 Factors in Melanoma Central Nervous System Metastases—A Cohort Study. Cancers *16*,
1091 2272.
1092 10. Winkler, F. (2015). The brain metastatic niche. Journal of Molecular Medicine *93*, 1213-1220.
1093 10.1007/s00109-015-1357-0.
1094 11. Wen, J., Li, Y., Deng, W., and Li, Z. (2025). Central nervous system and immune cells
1095 interactions in cancer: unveiling new therapeutic avenues. Frontiers in Immunology *Volume*
1096 *16 - 2025*. 10.3389/fimmu.2025.1528363.
1097 12. Lin, X., Kang, K., Chen, P., Zeng, Z., Li, G., Xiong, W., Yi, M., and Xiang, B. (2024). Regulatory
1098 mechanisms of PD-1/PD-L1 in cancers. Molecular cancer *23*, 108. 10.1186/s12943-024-
1099 02023-w.
1100 13. Jerby-Arnon, L., Shah, P., Cuoco, M.S., Rodman, C., Su, M.J., Melms, J.C., Leeson, R., Kanodia,
1101 A., Mei, S., Lin, J.R., et al. (2018). A Cancer Cell Program Promotes T Cell Exclusion and
1102 Resistance to Checkpoint Blockade. Cell *175*, 984-997.e924. 10.1016/j.cell.2018.09.006.
1103 14. Tawbi, H.A., Forsyth, P.A., Hodi, F.S., Algazi, A.P., Hamid, O., Lao, C.D., Moschos, S.J., Atkins,
1104 M.B., Lewis, K., Postow, M.A., et al. (2021). Long-term outcomes of patients with active
1105 melanoma brain metastases treated with combination nivolumab plus ipilimumab
1106 (CheckMate 204): final results of an open-label, multicentre, phase 2 study. Lancet Oncol *22*,
1107 1692-1704. 10.1016/s1470-2045(21)00545-3.
1108 15. Liu, T., Zhou, L., Xiao, Y., Andl, T., and Zhang, Y. (2022). BRAF Inhibitors Reprogram Cancer-
1109 Associated Fibroblasts to Drive Matrix Remodeling and Therapeutic Escape in Melanoma.
1110 Cancer research *82*, 419-432. 10.1158/0008-5472.Can-21-0614.
1111 16. Auslander, N., Zhang, G., Lee, J.S., Frederick, D.T., Miao, B., Moll, T., Tian, T., Wei, Z., Madan,
1112 S., Sullivan, R.J., et al. (2018). Robust prediction of response to immune checkpoint blockade
1113 therapy in metastatic melanoma. Nat Med *24*, 1545-1549. 10.1038/s41591-018-0157-9.
1114 17. Huang, A.C., Orlowski, R.J., Xu, X., Mick, R., George, S.M., Yan, P.K., Manne, S., Kraya, A.A.,
1115 Wubbenhorst, B., Dorfman, L., et al. (2019). A single dose of neoadjuvant PD-1 blockade
1116 predicts clinical outcomes in resectable melanoma. Nat Med *25*, 454-461. 10.1038/s41591-
1117 019-0357-y.
1118 18. Boshuizen, J., Vredevoogd, D.W., Krijgsman, O., Ligtenberg, M.A., Blankenstein, S., de Bruijn,
1119 B., Frederick, D.T., Kenski, J.C.N., Parren, M., Bruggemann, M., et al. (2020). Reversal of pre-
1120 existing NGFR-driven tumor and immune therapy resistance. Nat Commun *11*, 3946.
1121 10.1038/s41467-020-17739-8.
1122 19. Radke, J., Schumann, E., Onken, J., Koll, R., Acker, G., Bodnar, B., Senger, C., Tierling, S.,
1123 Möbs, M., Vajkoczy, P., et al. (2022). Decoding molecular programs in melanoma brain
1124 metastases. Nature Communications *13*, 7304. 10.1038/s41467-022-34899-x.
1125 20. In, G.K., Ribeiro, J.R., Yin, J., Xiu, J., Bustos, M.A., Ito, F., Chow, F., Zada, G., Hwang, L., Salama,
1126 A.K.S., et al. (2023). Multi-omic profiling reveals discrepant immunogenic properties and a
1127 unique tumor microenvironment among melanoma brain metastases. NPJ Precis Oncol *7*,
1128 120. 10.1038/s41698-023-00471-z.
1129 21. Kluger, H.M., Zito, C.R., Barr, M.L., Baine, M.K., Chiang, V.L.S., Sznol, M., Rimm, D.L., Chen, L.,
1130 and Jilaveanu, L.B. (2015). Characterization of PD-L1 Expression and Associated T-cell

Infiltrates in Metastatic Melanoma Samples from Variable Anatomic Sites. Clinical Cancer Research *21*, 3052-3060. 10.1158/1078-0432.Ccr-14-3073.

22. Kleffel, S., Posch, C., Barthel, S.R., Mueller, H., Schlapbach, C., Guenova, E., Elco, C.P., Lee, N., Juneja, V.R., Zhan, Q., et al. (2015). Melanoma Cell-Intrinsic PD-1 Receptor Functions Promote Tumor Growth. Cell *162*, 1242-1256. 10.1016/j.cell.2015.08.052.

23. Joyce, J.A., and Fearon, D.T. (2015). T cell exclusion, immune privilege, and the tumor microenvironment. Science *348*, 74-80. 10.1126/science.aaa6204.

24. Handel, E.E., McKeown, J., Wei, J., Kankaria, R.A., Burnette, H., Johnson, D.B., Lawless, A., Czapla, J., Sullivan, R.J., Albrecht, L.J., et al. (2025). Outcomes following long-term disease control with immune checkpoint inhibitors in patients with advanced melanoma. European journal of cancer *215*, 115171. https://doi.org/10.1016/j.ejca.2024.115171.

25. Margolin, K., Ernstoff, M.S., Hamid, O., Lawrence, D., McDermott, D., Puzanov, I., Wolchok, J.D., Clark, J.I., Sznol, M., Logan, T.F., et al. (2012). Ipilimumab in patients with melanoma and brain metastases: an open-label, phase 2 trial. Lancet Oncol *13*, 459-465. 10.1016/S1470-2045(12)70090-6.

26. Singh, C.R., Watanabe, R., Zhou, D., Jennings, M.D., Fukao, A., Lee, B., Ikeda, Y., Chiorini, J.A., Campbell, S.G., Ashe, M.P., et al. (2011). Mechanisms of translational regulation by a human eIF5-mimic protein. Nucleic Acids Res *39*, 8314-8328. 10.1093/nar/gkr339.

27. Zawerton, A., Yao, B., Yeager, J.P., Pippucci, T., Haseeb, A., Smith, J.D., Wischmann, L., Kühl, S.J., Dean, J.C.S., Pilz, D.T., et al. (2019). De Novo SOX4 Variants Cause a Neurodevelopmental Disease Associated with Mild Dysmorphism. Am J Hum Genet *104*, 246-259. 10.1016/j.ajhg.2018.12.014.

28. Ritz, U., and Seliger, B. (2001). The Transporter Associated With Antigen Processing (TAP): Structural Integrity, Expression, Function, and Its Clinical Relevance. Molecular Medicine *7*, 149-158. 10.1007/BF03401948.

29. Yoshihara, K., Shahmoradgoli, M., Martinez, E., Vegesna, R., Kim, H., Torres-Garcia, W., Trevino, V., Shen, H., Laird, P.W., Levine, D.A., et al. (2013). Inferring tumour purity and stromal and immune cell admixture from expression data. Nat Commun *4*, 2612. 10.1038/ncomms3612.

30. Manukyan, A., Bahry, E., Wyler, E., Becher, E., Pascual-Reguant, A., Plumbom, I., Dikmen, H.O., Elezkurtaj, S., Conrad, T., Altmüller, J., et al. (2023). VoltRon: A Spatial Omics Analysis Platform for Multi-Resolution and Multi-omics Integration using Image Registration. bioRxiv, 2023.2012.2015.571667. 10.1101/2023.12.15.571667.

31. Getis, A., and Ord, J.K. (1992). The Analysis of Spatial Association by Use of Distance Statistics. Geographical Analysis *24*, 189-206. https://doi.org/10.1111/j.1538-4632.1992.tb00261.x.

32. Hugo, W., Zaretsky, J.M., Sun, L., Song, C., Moreno, B.H., Hu-Lieskovan, S., Berent-Maoz, B., Pang, J., Chmielowski, B., Cherry, G., et al. (2017). Genomic and Transcriptomic Features of Response to Anti-PD-1 Therapy in Metastatic Melanoma. Cell *168*, 542. 10.1016/j.cell.2017.01.010.

33. Heng, Y., Zhu, X., Wu, Q., Lin, H., Ding, X., Tao, L., and Lu, L. (2023). High Expression of Tumor HLA-DR Predicts Better Prognosis and Response to Anti-PD-1 Therapy in Laryngeal Squamous Cell Carcinoma. Translational Oncology *33*, 101678. https://doi.org/10.1016/j.tranon.2023.101678.

34. Tabassum, A., Samdani, M.N., Dhali, T.C., Alam, R., Ahammad, F., Samad, A., and Karpiński, T.M. (2021). Transporter associated with antigen processing 1 (TAP1) expression and prognostic analysis in breast, lung, liver, and ovarian cancer. J Mol Med (Berl) *99*, 1293-1309. 10.1007/s00109-021-02088-w.

35. Holling, T.M., van der Stoep, N., Quinten, E., and van den Elsen, P.J. (2002). Activated Human T Cells Accomplish MHC Class II Expression Through T Cell-Specific Occupation of Class II Transactivator Promoter III1. The Journal of Immunology *168*, 763-770. 10.4049/jimmunol.168.2.763.

36. Van Kaer, L., Ashton-Rickardt, P.G., Ploegh, H.L., and Tonegawa, S. (1992). TAP1 mutant mice are deficient in antigen presentation, surface class I molecules, and CD4-8+ T cells. Cell *71*, 1205-1214. 10.1016/s0092-8674(05)80068-6.
37. Ling, A., Löfgren-Burström, A., Larsson, P., Li, X., Wikberg, M.L., Öberg, Å., Stenling, R., Edin, S., and Palmqvist, R. (2017). TAP1 down-regulation elicits immune escape and poor prognosis in colorectal cancer. Oncoimmunology *6*, e1356143. 10.1080/2162402x.2017.1356143.
38. Dhatchinamoorthy, K., Colbert, J.D., and Rock, K.L. (2021). Cancer Immune Evasion Through Loss of MHC Class I Antigen Presentation. Front Immunol *12*, 636568. 10.3389/fimmu.2021.636568.
39. Min, W., Pober, J.S., and Johnson, D.R. (1996). Kinetically coordinated induction of TAP1 and HLA class I by IFN-gamma: the rapid induction of TAP1 by IFN-gamma is mediated by Stat1 alpha. J Immunol *156*, 3174-3183.
40. Kanatani, S., Kreutzmann, J.C., Li, Y., West, Z., Larsen, L.L., Nikou, D.V., Eidhof, I., Walton, A., Zhang, S., Rodríguez-Kirby, L.R., et al. (2024). Whole-brain spatial transcriptional analysis at cellular resolution. Science *386*, 907-915. doi:10.1126/science.adn9947.
41. Heise, R., Amann, P.M., Ensslen, S., Marquardt, Y., Czaja, K., Joussen, S., Beer, D., Abele, R., Plewnia, G., Tampé, R., et al. (2016). Interferon Alpha Signalling and Its Relevance for the Upregulatory Effect of Transporter Proteins Associated with Antigen Processing (TAP) in Patients with Malignant Melanoma. PloS one *11*, e0146325. 10.1371/journal.pone.0146325.
42. Cramer, L.A., Nelson, S.L., and Klemsz, M.J. (2000). Synergistic induction of the Tap-1 gene by IFN-gamma and lipopolysaccharide in macrophages is regulated by STAT1. J Immunol *165*, 3190-3197. 10.4049/jimmunol.165.6.3190.
43. Luskin, M.R., Murakami, M.A., Manalis, S.R., and Weinstock, D.M. (2018). Targeting minimal residual disease: a path to cure? Nat Rev Cancer *18*, 255-263. 10.1038/nrc.2017.125.
44. Rambow, F., Rogiers, A., Marin-Bejar, O., Aibar, S., Femel, J., Dewaele, M., Karras, P., Brown, D., Chang, Y.H., Debiec-Rychter, M., et al. (2018). Toward Minimal Residual Disease-Directed Therapy in Melanoma. Cell *174*, 843-855 e819. 10.1016/j.cell.2018.06.025.
45. Lehmann, J., Caduff, N., Krzywinska, E., Stierli, S., Salas-Bastos, A., Loos, B., Levesque, M.P., Dummer, R., Stockmann, C., Munz, C., et al. (2023). Escape from NK cell tumor surveillance by NGFR-induced lipid remodeling in melanoma. Sci Adv *9*, eadc8825. 10.1126/sciadv.adc8825.
46. Busselaar, J., Sijbranda, M., and Borst, J. (2024). The importance of type I interferon in orchestrating the cytotoxic T-cell response to cancer. Immunology Letters *270*, 106938. https://doi.org/10.1016/j.imlet.2024.106938.
47. Nguyen, T.H., Kumar, D., Prince, C., Martini, D., Grunwell, J.R., Lawrence, T., Whitely, T., Chappelle, K., Chonat, S., Prahalad, S., et al. (2024). Frequency of HLA-DR⁺CD38^{hi} T cells identifies and quantifies T-cell activation in hemophagocytic lymphohistiocytosis, hyperinflammation, and immune regulatory disorders. Journal of Allergy and Clinical Immunology *153*, 309-319. 10.1016/j.jaci.2023.07.008.
48. Prinz, M., Jung, S., and Priller, J. (2019). Microglia Biology: One Century of Evolving Concepts. Cell *179*, 292-311. 10.1016/j.cell.2019.08.053.
49. Doron, H., Pukrop, T., and Erez, N. (2019). A Blazing Landscape: Neuroinflammation Shapes Brain Metastasis. Cancer Res *79*, 423-436. 10.1158/0008-5472.Can-18-1805.
50. Henrik Heiland, D., Ravi, V.M., Behringer, S.P., Frenking, J.H., Wurm, J., Joseph, K., Garrelfs, N.W.C., Strähle, J., Heynckes, S., Grauvogel, J., et al. (2019). Tumor-associated reactive astrocytes aid the evolution of immunosuppressive environment in glioblastoma. Nature Communications *10*, 2541. 10.1038/s41467-019-10493-6.
51. Zamanian, J.L., Xu, L., Foo, L.C., Nouri, N., Zhou, L., Giffard, R.G., and Barres, B.A. (2012). Genomic Analysis of Reactive Astrogliosis. The Journal of Neuroscience *32*, 6391-6410. 10.1523/jneurosci.6221-11.2012.

52. Lawrence, J.M., Schardien, K., Wigdahl, B., and Nonnemacher, M.R. (2023). Roles of neuropathology-associated reactive astrocytes: a systematic review. Acta Neuropathologica Communications *11*, 42. 10.1186/s40478-023-01526-9.
53. Jurga, A.M., Paleczna, M., Kadluczka, J., and Kuter, K.Z. (2021). Beyond the GFAP-Astrocyte Protein Markers in the Brain. Biomolecules *11*. 10.3390/biom11091361.
54. Sofroniew, M.V. (2020). Astrocyte Reactivity: Subtypes, States, and Functions in CNS Innate Immunity. Trends Immunol *41*, 758-770. 10.1016/j.it.2020.07.004.
55. Landsberg, J., Kohlmeyer, J., Renn, M., Bald, T., Rogava, M., Cron, M., Fatho, M., Lennerz, V., Wolfel, T., Holzel, M., and Tuting, T. (2012). Melanomas resist T-cell therapy through inflammation-induced reversible dedifferentiation. Nature *490*, 412-416. 10.1038/nature11538.
56. Roukens, M.G., Frederiks, C.L., Seinstra, D., Braccioli, L., Khalil, A.A., Pals, C., De Neck, S., Bornes, L., Beerling, E., Mokry, M., et al. (2021). Regulation of a progenitor gene program by SOX4 is essential for mammary tumor proliferation. Oncogene *40*, 6343-6353. 10.1038/s41388-021-02004-z.
57. Liu, Y., John, P., Nishitani, K., Cui, J., Nishimura, C.D., Christin, J.R., Couturier, N., Ren, X., Wei, Y., Pulanco, M.C., et al. (2023). A SOX9-B7x axis safeguards dedifferentiated tumor cells from immune surveillance to drive breast cancer progression. Developmental cell *58*, 2700-2717.e2712. 10.1016/j.devcel.2023.10.010.
58. Tsang, S.M., Oliemuller, E., and Howard, B.A. (2020). Regulatory roles for SOX11 in development, stem cells and cancer. Seminars in cancer biology *67*, 3-11. https://doi.org/10.1016/j.semcancer.2020.06.015.
59. Yu, B., Chen, L., Zhang, W., Li, Y., Zhang, Y., Gao, Y., Teng, X., Zou, L., Wang, Q., Jia, H., et al. (2020). TOP2A and CENPF are synergistic master regulators activated in cervical cancer. BMC Medical Genomics *13*, 145. 10.1186/s12920-020-00800-2.
60. Zhao, H.C., Chen, C.Z., Tian, Y.Z., Song, H.Q., Wang, X.X., Li, Y.J., He, J.F., and Zhao, H.L. (2023). CD168(+) macrophages promote hepatocellular carcinoma tumor stemness and progression through TOP2A/β-catenin/YAP1 axis. iScience *26*, 106862. 10.1016/j.isci.2023.106862.
61. Zhang, Y., and Lv, X. (2025). IGFBP3 modulation of tumor pathogenesis and cell signaling pathways (Review). Oncol Lett *30*, 379. 10.3892/ol.2025.15125.
62. Becker, M.A., Hou, X., Harrington, S.C., Weroha, S.J., Gonzalez, S.E., Jacob, K.A., Carboni, J.M., Gottardis, M.M., and Haluska, P. (2012). IGFBP ratio confers resistance to IGF targeting and correlates with increased invasion and poor outcome in breast tumors. Clin Cancer Res *18*, 1808-1817. 10.1158/1078-0432.Ccr-11-1806.
63. Muller, F., Scherer, M., Assenov, Y., Lutsik, P., Walter, J., Lengauer, T., and Bock, C. (2019). RnBeads 2.0: comprehensive analysis of DNA methylation data. Genome Biol *20*, 55. 10.1186/s13059-019-1664-9.
64. Pidsley, R., Y Wong, C.C., Volta, M., Lunnon, K., Mill, J., and Schalkwyk, L.C. (2013). A data-driven approach to preprocessing Illumina 450K methylation array data. BMC Genomics *14*, 293. 10.1186/1471-2164-14-293.
65. Daenekas, B., Pérez, E., Boniolo, F., Stefan, S., Benfatto, S., Sill, M., Sturm, D., Jones, D.T.W., Capper, D., Zapatka, M., and Hovestadt, V. (2024). Conumee 2.0: enhanced copy-number variation analysis from DNA methylation arrays for humans and mice. Bioinformatics *40*. 10.1093/bioinformatics/btae029.
66. Hao, Y., Hao, S., Andersen-Nissen, E., Mauck, W.M., 3rd, Zheng, S., Butler, A., Lee, M.J., Wilk, A.J., Darby, C., Zager, M., et al. (2021). Integrated analysis of multimodal single-cell data. Cell *184*, 3573-3587 e3529. 10.1016/j.cell.2021.04.048.
67. Korsunsky, I., Millard, N., Fan, J., Slowikowski, K., Zhang, F., Wei, K., Baglaenko, Y., Brenner, M., Loh, P.-r., and Raychaudhuri, S. (2019). Fast, sensitive and accurate integration of single-cell data with Harmony. Nature methods *16*, 1289-1296. 10.1038/s41592-019-0619-0.

1284 68. Pielawski, N., Andersson, A., Avenel, C., Behanova, A., Chelebian, E., Klemm, A., Nysjö, F.,
1285 Solorzano, L., and Wählby, C. (2023). TissUUmaps 3: Improvements in interactive
1286 visualization, exploration, and quality assessment of large-scale spatial omics data. Heliyon *9*,
1287 e15306. https://doi.org/10.1016/j.heliyon.2023.e15306.
1288 69. Love, M.I., Huber, W., and Anders, S. (2014). Moderated estimation of fold change and
1289 dispersion for RNA-seq data with DESeq2. Genome Biol *15*, 550. 10.1186/s13059-014-0550-8.
1290 70. Redmer, T., Schumann, E., Peters, K., Weidemeier, M.E., Nowak, S., Schroeder, H.W.S., Vidal,
1291 A., Radbruch, H., Lehmann, A., Kreuzer-Redmer, S., et al. (2024). MET receptor serves as a
1292 promising target in melanoma brain metastases. Acta Neuropathol *147*, 44. 10.1007/s00401-
1293 024-02694-1.
1294 71. de Visser, K.E., and Joyce, J.A. (2023). The evolving tumor microenvironment: From cancer
1295 initiation to metastatic outgrowth. Cancer cell *41*, 374-403. 10.1016/j.ccell.2023.02.016.
1296 72. Passaro, A.P., Lebos, A.L., Yao, Y., and Stice, S.L. (2021). Immune Response in Neurological
1297 Pathology: Emerging Role of Central and Peripheral Immune Crosstalk. Front Immunol *12*,
1298 676621. 10.3389/fimmu.2021.676621.
1299 73. Sofroniew, M.V. (2009). Molecular dissection of reactive astrogliosis and glial scar formation.
1300 Trends Neurosci *32*, 638-647. 10.1016/j.tins.2009.08.002.
1301 74. Li, J., and Stanger, B.Z. (2020). How Tumor Cell Dedifferentiation Drives Immune Evasion and
1302 Resistance to Immunotherapy. Cancer Res *80*, 4037-4041. 10.1158/0008-5472.Can-20-1420.
1303 75. Biermann, J., Melms, J.C., Amin, A.D., Wang, Y., Caprio, L.A., Karz, A., Tagore, S., Barrera, I.,
1304 Ibarra-Arellano, M.A., Andreatta, M., et al. (2022). Dissecting the treatment-naive ecosystem
1305 of human melanoma brain metastasis. Cell *185*, 2591-2608 e2530.
1306 10.1016/j.cell.2022.06.007.
1307 76. Vervoort, S.J., Lourenço, A.R., van Boxtel, R., and Coffer, P.J. (2013). SOX4 Mediates TGF-β-
1308 Induced Expression of Mesenchymal Markers during Mammary Cell Epithelial to
1309 Mesenchymal Transition. PloS one *8*, e53238. 10.1371/journal.pone.0053238.
1310 77. Andreev, D.E., Loughran, G., Fedorova, A.D., Mikhaylova, M.S., Shatsky, I.N., and Baranov,
1311 P.V. (2022). Non-AUG translation initiation in mammals. Genome Biol *23*, 111.
1312 10.1186/s13059-022-02674-2.
1313 78. Li, C., Li, Q., Li, L., Sun, S., and Lei, X. (2024). The Prognostic and Immune Significance of
1314 BZW2 in Pan-Cancer and its Relationship with Proliferation and Apoptosis of Cervical Cancer.
1315 FBL *29*. 10.31083/j.fbl2903097.
1316 79. Garcia-Diaz, A., Shin, D.S., Moreno, B.H., Saco, J., Escuin-Ordinas, H., Rodriguez, G.A.,
1317 Zaretsky, J.M., Sun, L., Hugo, W., Wang, X., et al. (2017). Interferon Receptor Signaling
1318 Pathways Regulating PD-L1 and PD-L2 Expression. Cell reports *19*, 1189-1201.
1319 https://doi.org/10.1016/j.celrep.2017.04.031.
1320 80. Yoshihama, S., Vijayan, S., Sidiq, T., and Kobayashi, K.S. (2017). NLRC5/CITA: A Key Player in
1321 Cancer Immune Surveillance. Trends Cancer *3*, 28-38.
1322 https://doi.org/10.1016/j.trecan.2016.12.003.
1323 81. Ayers, M., Lunceford, J., Nebozhyn, M., Murphy, E., Loboda, A., Kaufman, D.R., Albright, A.,
1324 Cheng, J.D., Kang, S.P., Shankaran, V., et al. (2017). IFN-γ–related mRNA profile predicts
1325 clinical response to PD-1 blockade. The Journal of clinical investigation *127*, 2930-2940.
1326 10.1172/JCI91190.
1327 82. Niknafs, N., Balan, A., Cherry, C., Hummelink, K., Monkhorst, K., Shao, X.M., Belcaid, Z.,
1328 Marrone, K.A., Murray, J., Smith, K.N., et al. (2023). Persistent mutation burden drives
1329 sustained anti-tumor immune responses. Nat Med *29*, 440-449. 10.1038/s41591-022-02163-
1330 w.

1331

Single cell spatial Transcriptomic

Associated single cell studies

Immune resistance program

Melanoma (GSE115978)

post treatment n=10 patients

treatment naive n=13 patients

MBM (GSE200218)

Associated bulk studies

Melanoma (Liu et al.)

MBM (EGAS00001005975)

ICi (Nivolumab, Pembrolizumab)
ICi (Nivolumab, Ipilimumab)
Treatment naive

Spatial single cell profiling (MBM)

1 TMA Preparation

TMA

TMA (n=16 specimen)

H&E
DAPI
Cell types
Probe/ transcript counts
Molecules

Xenium (10X) Imaging and signal processing

2 Subgroups

CNS cluster
Ecad^{high}
De-differentiated NGFR^{high}
UMAP_2
UMAP_1
BZW2^{high} and/or SOX4^{high}

SOX4
BZW2
Immune score
Immune hot areas
high
low

3 Immune resistance program

Immune niches: Immunogenic (hot) Suppressive (cold)

Niche-determining factors

Log2FC (FDR<0.05)

TAP1 SOX6 SOX4 NKG7 NGFR MX1 MET LGALS9 ITGB7 IGFBP3 GZMA GNLY CD8A CCL5 C1QC BZW2

Spatial immune niches predict response to therapy and survival

BZW2^{high}
TAP1^{high}
ImmuneScore
high
low

ICi

TAP1^{high}/BZW2^{low}/ SOX4^{low}

TAP1^{low}/BZW2^{high}/ SOX4^{high}

Survival probability (TCGA-SKCM, n=459)

HR(BZW2) = 1.355
HR(TAP1) = 0.485
Logrank P = 7.3 x 10^{-7}

BZW2^{low}/TAP1^{high}
BZW2^{high}/TAP1^{low}

Figure 1

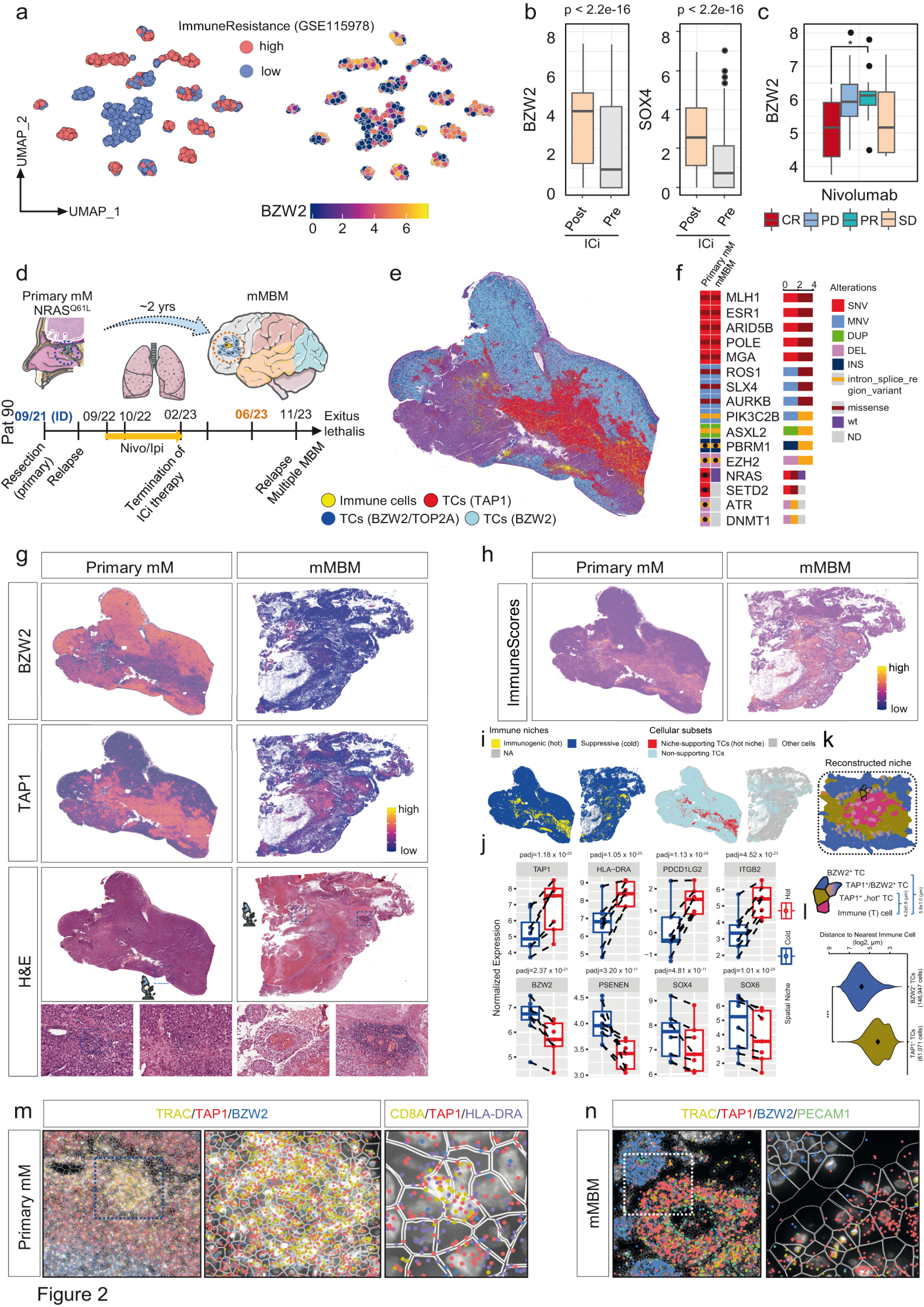
a
ImmuneResistance (GSE115978)
high
low
UMAP_2
UMAP_1
BZW2
0 2 4 6
b
p < 2.2e-16
p < 2.2e-16
BZW2
SOX4
Post
Pre
ICi
c
BZW2
Nivolumab
CR PD PR SD
d
Primary mM
NRAS Q61L
~2 yrs
mMBM
Pat 90
09/21 (ID)
09/22 10/22
02/23
06/23
11/23
Exitus lethalis
Nivo/Ipi
Resection (primary)
Relapse
Termination of ICi therapy
Relapse Multiple MBM
e
Immune cells
TCs (TAP1)
TCs (BZW2/TOP2A)
TCs (BZW2)
f
Primary mM
mMBM
MLH1
ESR1
ARID5B
POLE
MGA
ROS1
SLX4
AURKB
PIK3C2B
ASXL2
PBRM1
EZH2
NRAS
SETD2
ATR
DNMT1
Alterations
SNV
MNV
DUP
DEL
INS
intron_splice_region_variant
missense
wt
ND
g
Primary mM
mMBM
BZW2
TAP1
H&E
high
low
h
Primary mM
mMBM
ImmuneScores
high
low
i
Immune niches
Immunogenic (hot)
Suppressive (cold)
NA
Cellular subsets
Niche-supporting TCs (hot niche)
Non-supporting TCs
Other cells
k
Reconstructed niche
j
TAP1
HLA-DRA
PDCD1LG2
ITGB2
BZW2
PSENEN
SOX4
SOX6
Normalized Expression
Hot
Cold
Spatial Niche
l
BZW2+ TC
TAP1+/BZW2+ TC
TAP1+ „hot" TC
Immune (T) cell
Distance to Nearest Immune Cell (log2, µm)
m
TRAC/TAP1/BZW2
CD8A/TAP1/HLA-DRA
Primary mM
n
TRAC/TAP1/BZW2/PECAM1
mMBM

Figure 2

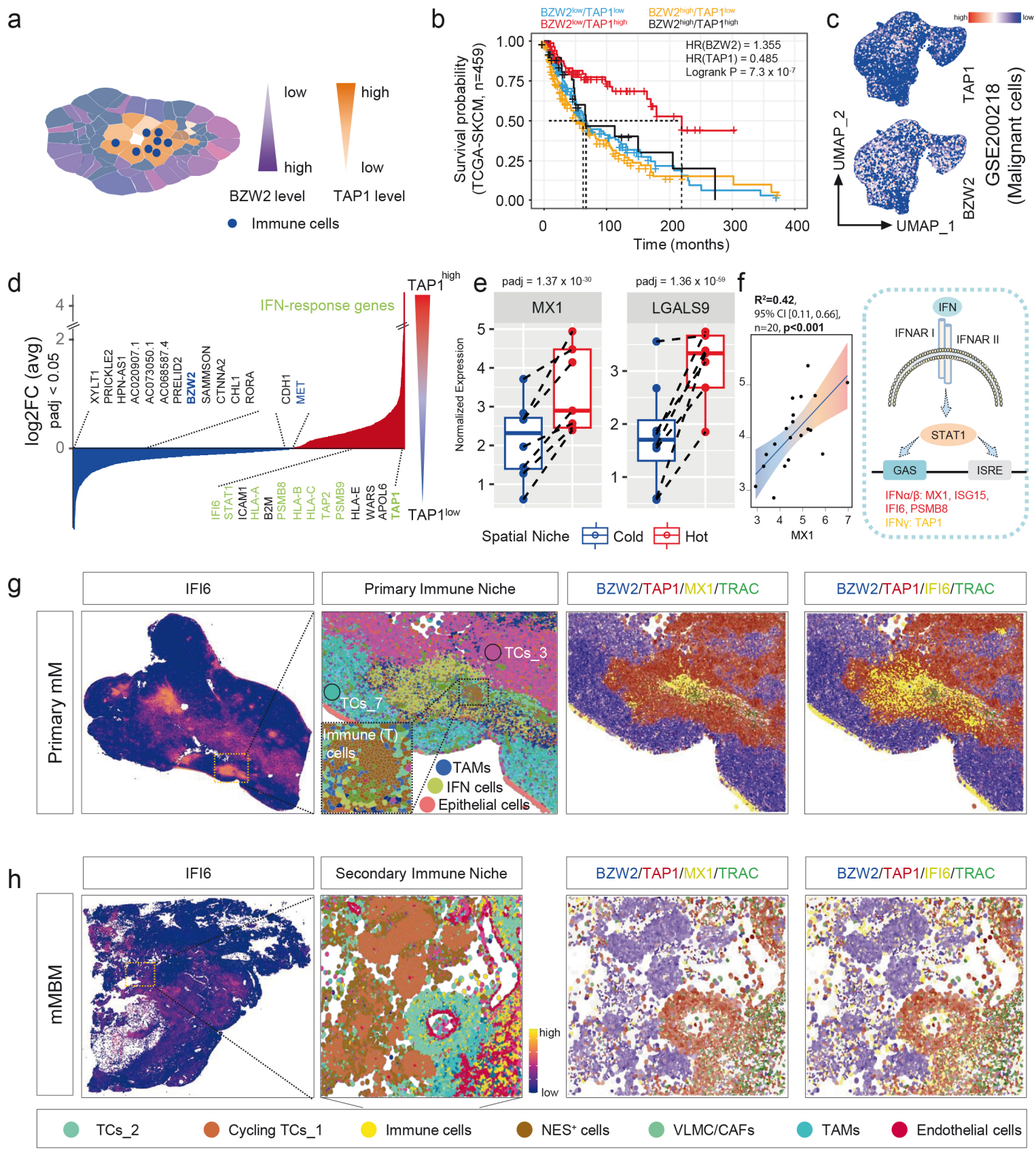
a
low
high
high
low
BZW2 level
TAP1 level
Immune cells
b
BZW2low/TAP1low
BZW2low/TAP1high
BZW2high/TAP1low
BZW2high/TAP1high
HR(BZW2) = 1.355
HR(TAP1) = 0.485
Logrank P = 7.3 x 10-7
Survival probability (TCGA-SKCM, n=459)
Time (months)
c
high
low
TAP1
BZW2
UMAP_2
UMAP_1
GSE200218 (Malignant cells)
d
log2FC (avg)
padj < 0.05
IFN-response genes
TAP1high
TAP1low
XYLT1
PRICKLE2
HPN-AS1
AC020907.1
AC073050.1
AC068587.4
PRELID2
BZW2
SAMMSON
CTNNA2
CHL1
RORA
CDH1
MET
IFI6
STAT1
ICAM1
HLA-A
B2M
PSMB8
HLA-B
HLA-C
TAP2
PSMB9
HLA-E
WARS
APOL6
TAP1
e
padj = 1.37 x 10-30
padj = 1.36 x 10-59
MX1
LGALS9
Normalized Expression
Spatial Niche
Cold
Hot
f
R²=0.42,
95% CI [0.11, 0.66],
n=20, p<0.001
MX1
IFN
IFNAR I
IFNAR II
STAT1
GAS
ISRE
IFNα/β: MX1, ISG15, IFI6, PSMB8
IFNγ: TAP1
g
IFI6
Primary Immune Niche
BZW2/TAP1/MX1/TRAC
BZW2/TAP1/IFI6/TRAC
Primary mM
TCs_3
TCs_7
Immune (T) cells
TAMs
IFN cells
Epithelial cells
h
IFI6
Secondary Immune Niche
BZW2/TAP1/MX1/TRAC
BZW2/TAP1/IFI6/TRAC
mMBM
high
low
TCs_2
Cycling TCs_1
Immune cells
NES+ cells
VLMC/CAFs
TAMs
Endothelial cells
i
BZW2/TAP1/STAT1
STAT1
MET/TAP1
mMBM
Primary mM
mMBM
mMBM

Figure 3

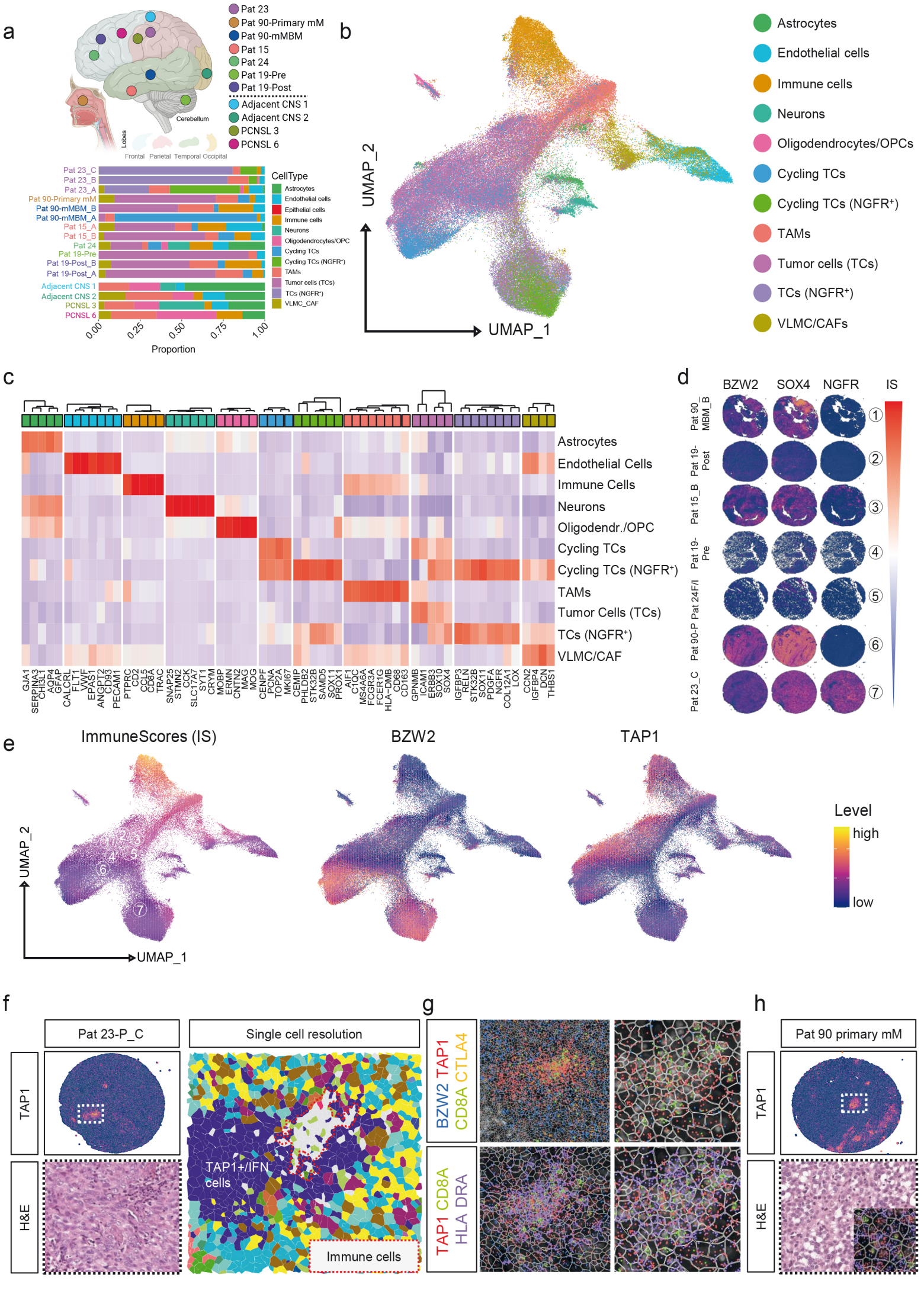
a
Pat 23
Pat 90-Primary mM
Pat 90-mMBM
Pat 15
Pat 24
Pat 19-Pre
Pat 19-Post
Adjacent CNS 1
Adjacent CNS 2
PCNSL 3
PCNSL 6
Cerebellum
Lobes
Frontal Parietal Temporal Occipital
CellType
Astrocytes
Endothelial cells
Epithelial cells
Immune cells
Neurons
Oligodendrocytes/OPC
Cycling TCs
Cycling TCs (NGFR+)
TAMs
Tumor cells (TCs)
TCs (NGFR+)
VLMC_CAF
Proportion
b
UMAP_2
UMAP_1
Astrocytes
Endothelial cells
Immune cells
Neurons
Oligodendrocytes/OPCs
Cycling TCs
Cycling TCs (NGFR+)
TAMs
Tumor cells (TCs)
TCs (NGFR+)
VLMC/CAFs
c
Astrocytes
Endothelial Cells
Immune Cells
Neurons
Oligodendr./OPC
Cycling TCs
Cycling TCs (NGFR+)
TAMs
Tumor Cells (TCs)
TCs (NGFR+)
VLMC/CAF
d
BZW2
SOX4
NGFR
IS
Pat 90 MBM_B
Pat 19-Post
Pat 15_B
Pat 19-Pre
Pat 24F/I
Pat 90-P
Pat 23_C
e
ImmuneScores (IS)
BZW2
TAP1
UMAP_2
UMAP_1
Level
high
low
f
Pat 23-P_C
Single cell resolution
TAP1
H&E
TAP1+/IFN cells
Immune cells
g
BZW2 TAP1 CD8A CTLA4
TAP1 CD8A HLA DRA
h
Pat 90 primary mM
TAP1
H&E

Figure 4

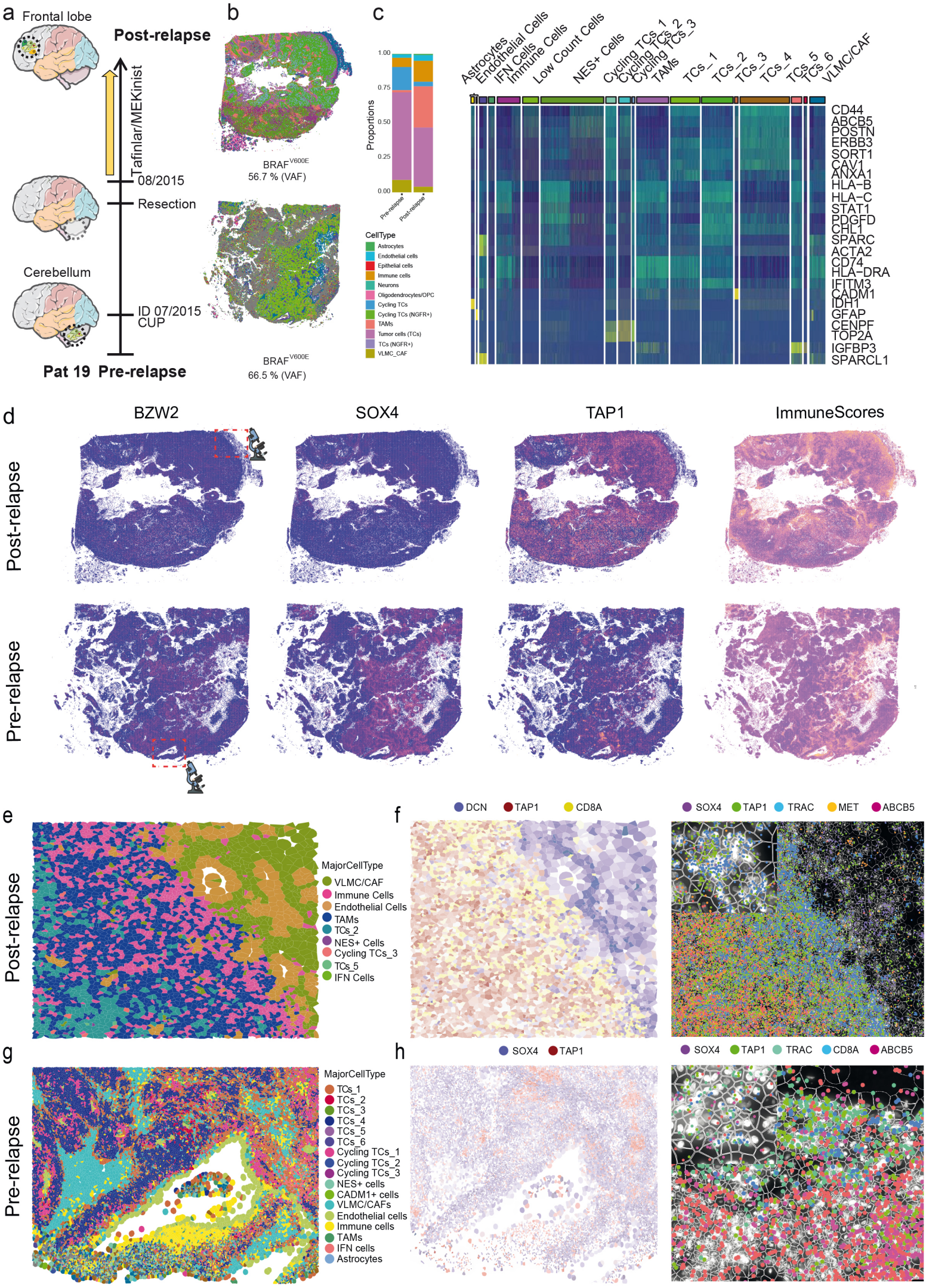
a
Frontal lobe
Post-relapse
Tafinlar/MEKinist
08/2015
Resection
Cerebellum
ID 07/2015
CUP
Pat 19 Pre-relapse
b
BRAF V600E
56.7 % (VAF)
BRAF V600E
66.5 % (VAF)
c
Proportions
Pre-relapse
Post-relapse
CellType
Astrocytes
Endothelial cells
Epithelial cells
Immune cells
Neurons
Oligodendrocytes/OPC
Cycling TCs
Cycling TCs (NGFR+)
TAMs
Tumor cells (TCs)
TCs (NGFR+)
VLMC_CAF
Astrocytes
Endothelial Cells
IFN Cells
Immune Cells
Low Count Cells
NES+ Cells
Cycling TCs_1
Cycling TCs_2
Cycling TCs_3
TAMs
TCs_1
TCs_2
TCs_3
TCs_4
TCs_5
TCs_6
VLMC/CAF
CD44
ABCB5
POSTN
ERBB3
SORT1
CAV1
ANXA1
HLA-B
HLA-C
STAT1
PDGFD
CHL1
SPARC
ACTA2
CD74
HLA-DRA
IFITM3
CADM1
IDH1
GFAP
CENPF
TOP2A
IGFBP3
SPARCL1
d
BZW2
SOX4
TAP1
ImmuneScores
Post-relapse
Pre-relapse
e
Post-relapse
MajorCellType
VLMC/CAF
Immune Cells
Endothelial Cells
TAMs
TCs_2
NES+ Cells
Cycling TCs_3
TCs_5
IFN Cells
f
DCN
TAP1
CD8A
SOX4
TAP1
TRAC
MET
ABCB5
g
Pre-relapse
MajorCellType
TCs_1
TCs_2
TCs_3
TCs_4
TCs_5
TCs_6
Cycling TCs_1
Cycling TCs_2
Cycling TCs_3
NES+ cells
CADM1+ cells
VLMC/CAFs
Endothelial cells
Immune cells
TAMs
IFN cells
Astrocytes
h
SOX4
TAP1
SOX4
TAP1
TRAC
CD8A
ABCB5

Figure 5